

8-2023

Evaluating How Well Active Fault Mapping Predicts earthquake surface-rupture locations

Chelsea Scott
Arizona State University

Ramon Arrowsmith
Arizona State University

Rachel Adam
Arizona State University

Christopher Madugo
Pacific Gas and Electric

Joseph Powell
Arizona State University

See next page for additional authors

Follow this and additional works at: https://pdxscholar.library.pdx.edu/geology_fac



Part of the [Geology Commons](#)

Let us know how access to this document benefits you.

Citation Details

Scott, C., Adam, R., Arrowsmith, R., Madugo, C., Powell, J., Ford, J., ... & Ingersoll, S. (2023). Evaluating how well active fault mapping predicts earthquake surface-rupture locations. *Geosphere*, 19(4), 1128-1156.

This Article is brought to you for free and open access. It has been accepted for inclusion in Geology Faculty Publications and Presentations by an authorized administrator of PDXScholar. Please contact us if we can make this document more accessible: pdxscholar@pdx.edu.

Authors

Chelsea Scott, Ramon Arrowsmith, Rachel Adam, Christopher Madugo, Joseph Powell, John Ford, Brian Gray, Ashley Streig, and multiple additional authors

GEOSPHERE, v. 19, no. 4

<https://doi.org/10.1130/GES02611.1>

13 figures; 5 tables; 1 set of supplemental files

CORRESPONDENCE: cpscott1@asu.edu

CITATION: Scott, C., Adam, R., Arrowsmith, R., Madugo, C., Powell, J., Ford, J., Gray, B., Koehler, R., Thompson, S., Sarmiento, A., Dawson, T., Kottke, A., Young, E., Williams, A., Kozaci, O., Oskin, M., Burgette, R., Streig, A., Seitz, G., Page, W., Badin, C., Carnes, L., Gibling, J., McNeil, J., Graham, J., Chupik, D., and Ingersoll, S., 2023, Evaluating how well active fault mapping predicts earthquake surface-rupture locations: *Geosphere*, v. 19, no. 4, p. 1128–1156, <https://doi.org/10.1130/GES02611.1>.

Science Editor: Andrea Hampel
Associate Editor: James A. Spotila

Received 4 October 2022
Revision received 24 March 2023
Accepted 12 April 2023

Final version published online 20 July 2023



This paper is published under the terms of the CC-BY-NC license.

© 2023 The Authors

Evaluating how well active fault mapping predicts earthquake surface-rupture locations

Chelsea Scott¹, Rachel Adam¹, Ramon Arrowsmith¹, Christopher Madugo², Joseph Powell¹, John Ford¹, Brian Gray³, Rich Koehler⁴, Stephen Thompson³, Alexandra Sarmiento^{5,6}, Timothy Dawson⁷, Albert Kottke², Elaine Young⁸, Alana Williams¹, Ozgur Kozaci⁹, Michael Oskin⁸, Reed Burgette^{10,*}, Ashley Streig¹¹, Gordon Seitz⁷, William Page², Curtis Badin^{12,†}, Lorraine Carnes¹, Jacqueline Gibling¹, James McNeil⁴, Jenna Graham⁴, Daniel Chupik¹, and Sean Ingersoll⁴

¹School of Earth and Space Exploration, Arizona State University, Tempe, Arizona 85287, USA²Pacific Gas and Electric, Geosciences Department, San Francisco, California 94105, USA³Lettis Consultants International, Inc., Concord, California 94520, USA⁴Nevada Bureau of Mines and Geology, University of Nevada–Reno, 1664 N. Virginia Street, MS 178, Reno, Nevada 89557, USA⁵The B. John Garrick Institute for the Risk Sciences, University of California–Los Angeles, Los Angeles, California 90095, USA⁶GeoPentech, Inc., Irvine, California 92617, USA⁷Seismic Hazard Assessment Program, California Geological Survey, San Mateo, California 94403, USA⁸Department of Earth and Planetary Sciences, University of California–Davis, 462 Crocker Lane, Davis, California 95616, USA⁹Infra Terra, San Francisco, California 94103, USA¹⁰Department of Geological Sciences, New Mexico State University, Las Cruces, New Mexico 88003, USA¹¹Department of Geology, Portland State University, Portland, Oregon 97232, USA¹²Department of Geological Sciences, Stanford University, Stanford, California 94305-2115, USA

ABSTRACT

Earthquake surface-fault rupture location uncertainty is a key factor in fault displacement hazard analysis and informs hazard and risk mitigation strategies. Geologists often predict future rupture locations from fault mapping based on the geomorphology interpreted from remote-sensing data sets. However, surface processes can obscure fault location, fault traces may be mapped in error, and a future rupture may not break every fault trace. We assessed how well geomorphology-based fault mapping predicted surface ruptures for seven earthquakes: 1983 M 6.9 Borah Peak, 2004 M 6.0 Parkfield, 2010 M 7.2 El Mayor–Cucapah, 2011 M 6.7 Fukushima–Hamadori, 2014 M 6.0 South Napa, 2016 M 7.8 Kaikoura, and 2016 M 7 Kumamoto. We trained geoscience students to produce active fault maps using topography and imagery acquired before the earthquakes. A geologic professional completed a “control” map. Mappers used a new “geomorphic indicator ranking” approach to rank fault confidence based on geomorphologic landforms. We determined the accuracy of the mapped faults by comparing the fault maps to published rupture maps. We defined predicted ruptures as ruptures near a fault (50–200 m, depending on the fault confidence) that interacted with the landscape in a

similar way to the fault. The mapped faults predicted between 12% to 68% of the principal rupture length for the studied earthquakes. The median separation distances between predicted ruptures and strong, distinct, or weak faults were 15–30 m. Our work highlights that mapping future fault ruptures is an underappreciated challenge of fault displacement hazard analysis—even for experts—with implications for risk management, engineering site assessments, and fault exclusion zones.

INTRODUCTION

In surface-rupturing earthquakes, fault displacement can damage infrastructure that crosses or overlies fault zones. Fault displacement is a particular concern for critical infrastructure such as nuclear facilities (Stepp et al., 2001; IAEA, 2021), gas and water pipelines (Honegger and Nyman, 2004; American Lifelines Alliance, 2005), roadways (Pamuk et al., 2005), and dams (Stirling et al., 2021). Though land-use regulation can mitigate the surface-rupture risk by prohibiting infrastructure near active faults (Kerr et al., 2003; Bryant and Hart, 2007; Boncio et al., 2012), structures required to cross active faults may need special engineering solutions to withstand surface-fault rupture (Woodward-Lundgren and Associates, 1974; Hall et al., 2003; Bray, 2001). Probabilistic fault displacement hazard analysis quantifies the annualized fault displacement hazard at a site, and this methodology requires statistical expressions of fault rupture location uncertainty relative to a mapped fault trace (Youngs et al., 2003; Petersen et al., 2011; Chen and Petersen, 2019; Nurminen et al.,

*Now at Oregon Department of Geology and Mineral Industries, Portland, Oregon 97232, USA.

†Now at Department of Earth and Planetary Science, University of California–Berkeley, Berkeley, California 94720-4767, USA.

Chelsea Scott <https://orcid.org/0000-0002-3884-4693>

2020). More broadly, accurately mapped faults also serve as important input into seismic hazard analyses that predict or forecast levels of ground shaking.

Mitigation associated with fault rupture requires accurately mapped faults and fault uncertainty zones that adequately predict future surface-rupture locations. Defining accurate fault uncertainty zones (often called fault rupture hazard zones in engineering practice) is important when the zone imposes a societal cost such as building restrictions in densely populated areas or expensive engineering solutions. Detailed field-based geologic mapping, geophysical surveys, and subsurface investigations are integral to accurately defining fault rupture hazard zones. However, collection of these data is not always logistically or financially practical. A key motivation for this study was to evaluate appropriate fault uncertainty zone widths based on regional mapping of landscape geomorphology in areas that lack extensive site-specific or field-based study.

The prediction of future coseismic rupture location from landscape geomorphology is built on the assumptions that the landscape preserves evidence of past fault activity and that this past activity is a good indicator of future seismic activity. Indeed, the use of geomorphology in active fault mapping is well established (Vedder and Wallace, 1970; Lienkaemper, 1992, 2006; Geological Survey of Japan, 1993; etc.). However, there has been little investigation into how well faults mapped from geomorphic criteria predict future earthquake rupture locations. In a study of historical strike-slip earthquakes in Southern California, Petersen et al. (2011) showed that faults mapped before an earthquake (abbreviated pre-rupture faults) were ~25–120 m away from the subsequent coseismic ruptures (abbreviated ruptures). Thompson Jobe et al. (2020) showed that 35% of the 2019 Ridgecrest sequence ruptures occurred along previously mapped faults, but that with a detailed inspection (and knowledge of the rupture pattern), 50%–70% of the ruptures could be recognized from pre-event remote-sensing data.

In this contribution, we assessed how well geomorphology-based fault mapping using remote-sensing data sets acquired before the earthquake of focus (i.e., pre-rupture fault mapping) predicted the subsequent surface ruptures for the 1983 M 6.9 Borah Peak, 2004 M 6.0 Parkfield, 2010 M 7.2 El Mayor–Cucupah, 2011 M 6.7 Fukushima–Hamadori, 2014 M 6.0 South Napa, 2016 M 7 Kumamoto, and 2016 M 7.8 Kaikoura earthquakes (Fig. 1). These earthquakes collectively represent multiple climate types as well as strike-slip and normal faulting regimes. Ideally, published pre-rupture, high-resolution fault maps would be readily available to compare with coseismic ruptures. However, a literature review did not identify suitable maps at an adequate scale and with a consistent classification scheme for trace activity and confidence. To generate consistently executed pre-rupture fault maps for past earthquakes, we taught students to produce high-quality pre-rupture fault maps (Savigear, 1965; McCalpin, 2009), as described in the next section. Students were required to have had no prior knowledge of the earthquake rupture. A geologic professional completed an additional “control” map for our experiment. We advanced the skills of the student mappers by training them in the basics of remote sensing and in morphologic, surficial geologic, and geomorphic mapping. To

systematize fault mapping, we developed the geomorphic indicator ranking (GIR) approach to explicitly rank fault confidence based on the geomorphic landforms (see Remote-Sensing Data Sets Used for the Pre-Rupture Fault Mapping section).

We designed our pre-rupture mapping strategy to minimize the importance of prior knowledge of the local geologic setting while working to produce professional-quality maps. Use of well-trained student mappers avoided the high cost as well as two bias types that likely would have been inescapable when producing maps completed by experts with decades of experience (Bond et al., 2007; Salisbury et al., 2015). Confirmation bias occurs when a mapper looks to support their results based on past experience and disregards conflicting observations. Anchoring bias is the failure to depart from initial ideas such as those about the tectonic setting or past knowledge of the earthquake. The controls in our approach avoided the possible biases introduced in cases where expert geologists have knowledge of the earthquakes to be studied retroactively (e.g., Thompson Jobe et al., 2020).

We determined if coseismic ruptures were predicted by the mapped pre-rupture faults by comparing the pre-rupture faults, coseismic ruptures, and landscape geomorphology. We showed that mapped pre-rupture faults predicted a range of 12%–68% of the principal coseismic ruptures, normalized by rupture length. Strong, distinct, and weak faults that successfully predicted rupture traces are within tens of meters of ruptures. Uncertain faults were 100–200 m from the predicted rupture traces. Differences between the mapped faults and coseismic rupture maps may reflect landscape misinterpretation, incomplete mapping of faults with limited or no landscape preservation, or random variability in rupture patterns between earthquakes. We conclude this article by discussing ways to improve fault mapping, with implications for site evaluation, regulatory zoning, and trenching. We demonstrate an application of our research to define fault uncertainty zones.

■ FAULT MAPPING INSTRUCTION

Teaching Fault Mapping Based on Landscape Geomorphology

We taught students to produce professional-level fault maps based on landscape geomorphology using an office-based approach and QGIS software (<https://www.qgis.org/en/site/>). We taught fault mapping to students in (1) a formal course and (2) a mentored research project.

Authors Scott, Arrowsmith, and Koehler served as the instructors of record for the virtual course, “Mapping tectonic faults from geomorphology,” which was listed at the undergraduate and graduate levels at Arizona State University (ASU) and University of Nevada–Reno in fall 2020. The prerequisites were structural geology and geomorphology classes and senior standing for the undergraduate students. All students were earning geoscience degrees. During the first month, the instructors shared lecturing responsibilities based on their expertise on fault types and geographic area. Students learned to make

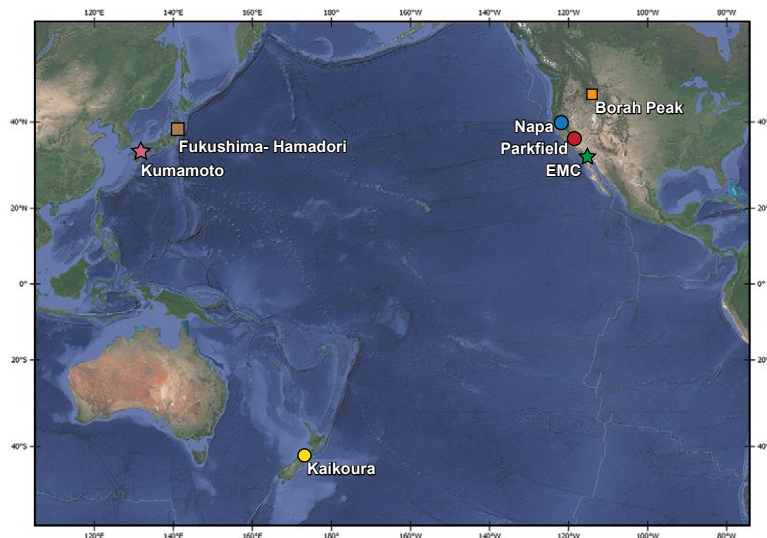


Figure 1. Pre-rupture fault mapping locations surrounding the Pacific Rim (top). The table (bottom) indicates the slip sense (N—normal, SS—strike slip), along-strike fault length of the completed pre-rupture fault mapping, climate, the availability of optical imagery and topography, and the mapper. DSM—digital surface model, DTM—digital terrain model and SRTM—30 m Shuttle Radar Topography Mission; F-H—Fukushima-Hamadori. EMC—El Mayor–Cucapah. “lidar” indicates the availability of a light detection and ranging (lidar)–derived DTM and/or DSM.

Earthquake	Symbol	Slip	Along strike fault length	Climate	Optical	Topography	Mapper
1983 M6.9 Borah Peak	Orange square	N	35 km	Semiarid	No	2 m DSM	3 students
2004 M6.0 Parkfield	Red circle	SS	41 km	Mediterranean	Yes	30 m SRTM	1 student
2010 M7.2 EMC	Green star	SS-N	55 km	Desert	Yes	6 m lidar	1 student
2011 M6.7 F-H	Brown square	N	11 km	Subtropical	Yes	2 m DTM	1 student
2014 M6.0 Napa	Blue circle	SS	25 km	Mediterranean	Yes	1 m lidar	1 student
2016 M7.0 Kumamoto	Pink star	SS-N	20 km	Subtropical	Yes	0.6 m lidar	1 consultant
2016 M7.8 Kaikoura	Yellow circle	SS	18 km	Coastal	Yes	1 m DTM	1 student

topographic derivatives such as hillshade and slope maps and were encouraged to frequently flip between all available remote-sensing data sets while mapping. Students learned to make observations by first mapping landscape morphology (i.e., convex, concave, flat areas, etc.) and shape (Saviegar, 1965) before making higher-order interpretations. The instructors emphasized the importance of “looking everywhere” and not leaving empty spaces in the first interpretive layer. Students honed their mapping skills through several assignments. They identified tectonic landforms (i.e., fault scarps, offset channels, triangular facets) in topographic hillshade maps and differentiated the relative ages of Quaternary units (surficial geology) in an arid climate. Students reviewed published fault maps, including those from Treiman and Bryant (2000), Witter et al. (2003), Cowgill et al. (2004), Sundermann and Kelson (2009), Brooks et al. (2011), Koe-hler et al. (2013), Coyan et al. (2013), and Toké et al. (2014).

In the last 2 mo of the course, each student completed two pre-rupture fault maps. These maps were for the 1966 and 2004 M 6.0 Parkfield, 1983 M 6.9 Borah Peak, 2010 M 7.2 El Mayor–Cucapah, 2011 M 6.7 Fukushima-Hamadori, 2013 M 7.7 Balochistan, 2014 M 6.0 South Napa, 2016 M 7 Kumamoto, and 2016 M 7.8 Kaikoura earthquakes. Students used remote-sensing data sets (see Remote-Sensing Data Sets Used for the Pre-Rupture Fault Mapping section) but did not consult other information such as geologic maps. Students assigned a ranking (i.e., primary or secondary fault; see “Geomorphic Indicator Ranking” section) and confidence level (i.e., strong, distinct, weak, or uncertain) to each fault trace. The students spent 20 h on each fault map, worked individually, and received feedback during a semiweekly class update and optional office hours. The instructors were cautious not to add interpretation reflecting prior knowledge of the earthquake. One of the maps (Borah Peak-1) was sufficiently

complete at the end of the course and suitable for the statistical evaluation in this publication. The other maps were not used in the subsequent analysis.

In spring 2021, three senior ASU undergraduate students who took the fall course completed fault maps for the 1983 Borah Peak (Borah Peak-2), 2004 Parkfield, 2010 El Mayor–Cucapah, 2011 Fukushima–Hamadori, 2014 Napa, and 2016 Kaikoura earthquakes (Fig. 1) in a mentored research project. Concurrently, a professional geologist completed the pre-rupture Kumamoto fault map using the same approach as the students. The students and professional geologist did not refer to the maps completed in the fall class because we wanted the fault maps to reflect the work of the individual mapper. The three students met weekly with Arrowsmith, Scott, and/or coauthor Gray to review progress and get feedback. During the spring 2022 iteration of the course, a senior graduate student completed a third Borah Peak map (Borah Peak-3). The three Borah Peak maps supported a test of mapping redundancy and were completed over almost the same area with small differences at the rupture ends. We archived the fault linework for the nine maps at the seven locations (Fig. 1) in the Supplemental Material¹.

Remote-Sensing Data Sets Used for the Pre-Rupture Fault Mapping

Our study included strike-slip, normal, and oblique-normal earthquakes surrounding the Pacific Rim (Fig. 1) and extended prior studies of strike-slip faults in Southern California (Petersen et al., 2011; Thompson Jobe et al., 2020). We focused on surface-rupturing earthquakes with approximately meter-scale publicly available imagery and/or topography data acquired before the earthquake of focus (i.e., pre-rupture data). We accessed pre-rupture imagery from Google Earth acquired via the time-button function. For the Parkfield, El Mayor–Cucapah, and Napa earthquakes, we mapped directly on topography derivative displayed in QGIS informed by observations from Google Earth. For the Kumamoto earthquake, we mapped on imagery from Google Earth georeferenced by the lead author (3.4 m error). We accessed light detection and ranging (lidar) and Shuttle Radar Mission Topography (SRTM; Farr et al., 2007) data from OpenTopography (<https://opentopography.org>). The 2000 30 m/pixel SRTM digital surface model (DSM) has a horizontal error ≤ 15 m (Rabus et al., 2003; Farr et al., 2007). For the El Mayor–Cucapah, Napa, and Kumamoto earthquakes, we visualized the landscape with and without vegetation from DSMs and digital terrain models (DTMs). The lidar data have ~ 25 – 75 cm horizontal error (Glennie, 2007; Goulden and Hopkinson, 2010; Scott et al., 2021). We used unpublished elevation data produced for the 1983 Borah Peak

¹Supplemental Material. Text file: Includes geomorphic indicator ranking feature table, full external mapping reviews, additional Borah Peak pre-rupture fault maps, a discussion of the one- and two-sided standard deviations of the rupture-to-fault separation distances, correlations between the fault mapping performance and different climate and fault metrics, and the readme for the ZIP. ZIP: Contains pre-rupture fault map linework for seven earthquakes saved as .shp files. Rupture linework files indicate pre-rupture mapping performance. Please visit <https://doi.org/10.1130/GEOS.S.22799552> to access the supplemental material, and contact editing@geosociety.org with any questions.

(Reitman et al., 2015), 2011 Fukushima–Hamadori (Nissen et al., 2014), and 2016 Kaikoura (Howell et al., 2020) earthquakes that were graciously shared by the respective authors. For Kaikoura, we produced a DTM (Isenburg, 2019) from a ground-classified point cloud with ± 2 m uncertainty.

Our data set selection differs from typical professional practice. Geoscience professionals often use published geologic maps as well as larger sets of Google Earth data and/or historical aerial (stereo) photography that capture seasonal vegetation changes, landscape colors and shading, and shadows. In addition, the mappers in our study conducted no field work during the mapping. While the mappers missed out on a local landscape calibration of the remote-sensing data sets, the mappers' knowledge of the rupture pattern from field work during the mapping process would no longer simulate pre-rupture mapping.

Geomorphic Indicator Ranking

Fault trace mapping is guided by geomorphology that reflects the interaction between surface and tectonic processes in sculpting the landscape (McCalpin, 2009). We developed the geomorphic indicator ranking (GIR) approach to standardize designation of fault confidence (i.e., strong, distinct, weak, or uncertain). We modeled our approach after Scharer et al. (2007), who assigned paleo-earthquake likelihood based on a consistent grading of the quality and quantity of paleoseismic evidence. We also found inspiration from other research: Salisbury et al. (2015) and Zielke et al. (2015) reviewed rating schemes for offset landforms and cumulative offset calculations. Lienkaemper (1992) ranked geomorphic features along the Hayward fault, California, according to clarity and summarized ranked features every 5 km. In the classic air-photo and field-based U.S. Geological Survey fault trace mapping of the San Andreas fault, Vedder and Wallace (1970) mapped geomorphic features (e.g., scarps, troughs, ridges, offset channels, sag ponds, and ponded alluvium) and fault traces. See Arrowsmith and Zielke (2009) for more discussion.

To implement the GIR, the students mapped geomorphic features and modifiers surrounding the fault traces, as shown in Figure 2, for a portion of the El Mayor–Cucapah earthquake. Geomorphic features included fault scarps from the most recent or older earthquakes and other tectonic geomorphology such as offset and beheaded drainages, triangular facets, or oversteepened range fronts. Modifiers such as landslides, aligned features, and anthropogenic alteration enhance or obscure fault evidence. Feature ranking (R) indicates fault evidence strength, where $R = 4$ is the highest and $R = 1$ is the lowest. For example, an offset drainage channel ($R = 4$) typically provides unequivocal evidence of strike-slip faulting (e.g., Wallace Creek along the San Andreas fault, California; Sieh and Jahns, 1984). A stream knickpoint ($R = 2$) only sometimes indicates faulting. Positive modifiers ($M = +1$) such as aligned features strengthen the fault interpretation. Negative modifiers ($M = -1$) such as roads and landslides across the fault lower confidence. Table S1 lists the ranked geomorphic features.

Panels

- A - Topographic hillshade from lidar
- B - Landsat/Copernicus optical imagery
- C - Geomorphic and GIR map
- D - Fault confidence ranking map

Geomorphic Mapping (Panel C)

- Simple Fault
- Drainages
- Ridges
- Anthropogenic Alteration

Geomorphic Indicator Ranking System (GIR) (Panel C)

- TF - Triangular Facet
- AFs - Single offset or cut Alluvial Fan
- Scp - Scarp
- DS - Deflected Stream
- SR - Shutter Ridge
- UO - Unit Offset
- AA - Anthropogenic Alteration
- Algmt - Alignment
- CrsCt - Cross Cut
- ER - Erosion
- LVD - Linear Valley/ Drainage
- ME - Morphologic Element
- Sdl - Saddle

Pre-rupture Fault Confidence Ranking (Panel D)

- Strong & Primary
- Distinct & Primary
- - - Weak & Primary
- - - Uncertain & Primary
- Distinct & Secondary
- - - Weak & Secondary
- Segment Spacing
- Mapping Boundary

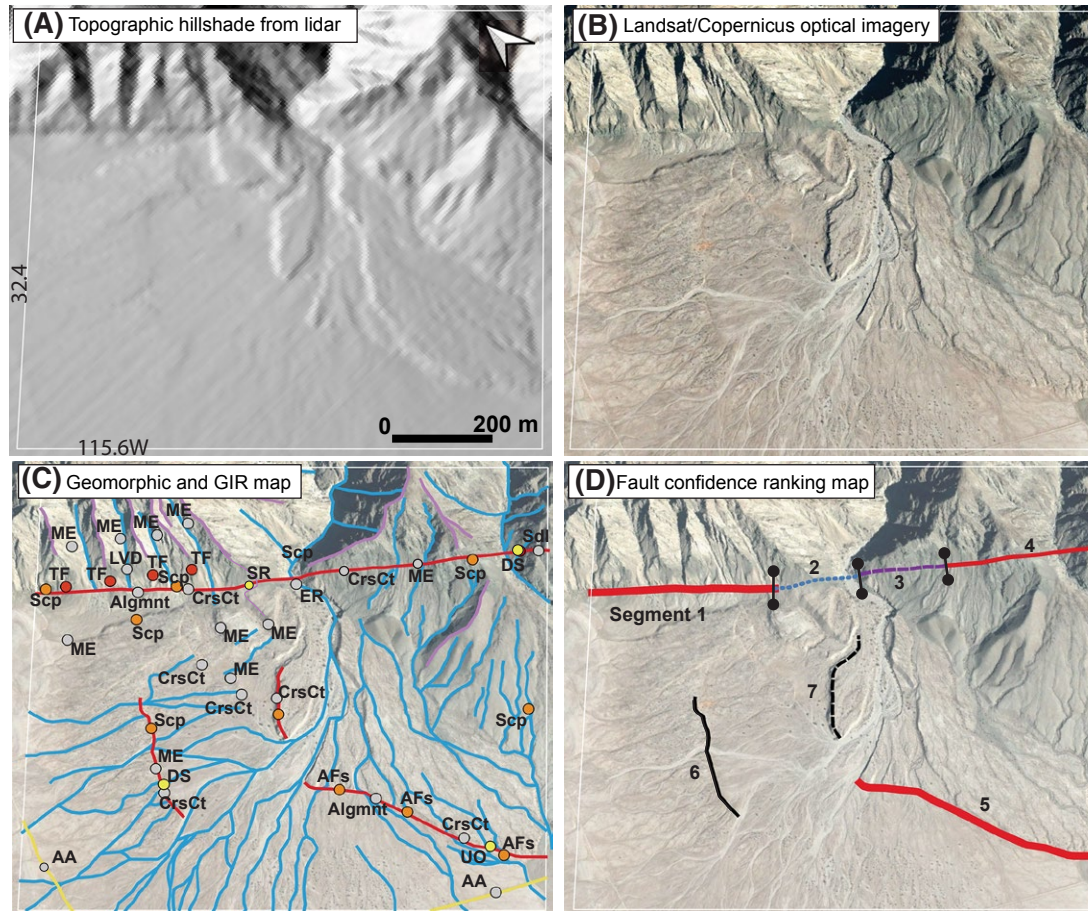


Figure 2. Geomorphic indicator ranking (GIR) along a portion of the 2010 El Mayor–Cucapah, Mexico, pre-rupture mapping: (A) 2006 topographic hillshade map, (B) Landsat/Copernicus optical imagery, (C) geomorphic mapping, ranked fault indicators, and modifiers, and (D) fault segments with segment number listed in the table below. (Bottom) Table of fault confidence calculations.

Segment #	Geomorphic Features	Segment Score	Scaled Score	Fault Confidence Ranking
1	4 Triangular Facets (Score = 4), 2 Scarp (3), 1 Alignment (+1), 4 Morphologic Elements (+1), 1 Cross Cut (+1), 1 Linear Valley/ Drainage (+1)	29	1	Strong
2	1 Shutter Ridge (2), 1 Erosion (-1)	1	4	Uncertain
3	1 Cross Cut (+1), 1 Morphologic Element (+1)	2	3	Weak
4	1 Scarp (3), 1 Deflected Stream (+1), 1 Saddle (+1)	5	2	Distinct
5	3 Single Offset or Cut Alluvial Fan (3), 1 Unit Offset (3), 1 Alignment (+1), 1 Cross Cut (+1)	14	1	Strong
6	1 Scarp (3), 1 Deflected Stream (2), 1 Cross Cut (+1), 1 Morphologic Element (+1)	7	2	Distinct
7	1 Scarp (3), 1 Cross Cut (+1)	4	3	Weak

Based on the geomorphology, we mapped fault traces as lines without a confidence level. We divided the fault traces into ~1-km-long segments with boundaries along geomorphic breaks (e.g., fault bends or indicator ranking changes). To calculate segment confidence, we summed geomorphic indicators along the fault segment:

$$\text{Segment confidence} = \sum_{i=0}^{\text{Total GIRs}} R_i + \sum_{j=0}^{\text{Total Modifiers}} M_j, \quad (1)$$

Our scaling ensured that fault confidence levels ranged from 1 to 4,

$$\text{Scaled score} = 5 - 3 * \frac{\text{segment confidence} - b}{a - b} - 1, \quad (2)$$

where *a* and *b* are the largest and smallest segment scores, respectively, for each mapping area. This scaled score flips the final score so that 1 is the highest.

We associated the 1–4 scaled scores with the language of strong, distinct, weak, and uncertain. Sometimes low-confidence faults are concealed (e.g., Petersen et al., 2011), implying an inferred fault trace buried under younger geologic or anthropogenic materials. This language does not apply here, because our scoring does not reflect precise geomorphic scenarios.

We distinguished principal and distributed faults (e.g., Nurminen et al., 2020, 2022; Sarmiento et al., 2021). A principal fault is the main,

often-continuous through-going fault that hosts the larger coseismic displacement and is expressed with a single-scarp, en echelon, branching, or anastomosing geometry (for examples, see Sarmiento et al., 2021). The fault can lack continuity across young surfaces if the mapper reasonably interprets continuity at depth. A distributed fault hosts less displacement than the primary fault, can be synthetic or antithetic to the primary fault, or can be fractures without displacement. We use the terms principal (for ruptures) and primary (for faults) synonymously, as well as the terms distributed (ruptures) and secondary (faults).

EXTERNAL EXPERT REVIEW OF THE PRE-RUPTURE MAPPING

We conducted an external expert review (Table 1) to assess if the student mapping was consistent with standards of practice. We used the expert's reviews in two ways: to explore if the reviewers' suggestions improved rupture prediction and to evaluate the correlation between the reviewer's rating fault map and rupture predictability performance.

We assigned the fault maps to academic and industry expert reviewers with no prior experience of the area. The experts viewed the same pre-rupture data sets as the students and did not review postevent references, geologic

TABLE 1. EXTERNAL PRE-RUPTURE FAULT MAPPING REVIEW SUMMARY

Earthquake name	Mapping complete?	Does geomorphology support fault mapping?	Certainty ranking consistent with geomorphology?	Average score
Borah Peak-2	2	1.5	2	1.8
	Needs revision/adequate: Some faults are mislocated near range fronts, often by tens to 300 m. Subtle fault scarps were missed, possibly due to not mapping at the full resolution of the data set.			
Parkfield	2	3	2.5	2.5
	Better than adequate: Good geomorphic mapping reinforces the location and fault trace confidence. Some missed traces.			
El Mayor–Cucapah	1	2	1	2
	Needs revision/adequate: Uneven mapping coverage. Faults adhered too closely to geomorphic features. Fault traces stop at older alluvial deposits instead of passing through them. Mapper misunderstood desert geomorphology.			
Fukushima	1.5	1.5	1	1.6
	Needs revision: Some fault scarps were misidentified near agriculture, leading to tens of meters in fault location error. Good trace continuity near development.			
Napa	2	2	1.5	1.8
	Adequate: Some missed secondary faults. Some faults are likely erosional or terrace formations and are too continuous given the area's erosion.			
Kumamoto	3	2	3	2.7
	Adequate: Overall good mapping. Some mapped tectonic scarps may only be erosional. Some inaccurate fault placement.			
Kaikoura	2	2	2	2
	Adequate: Primary traces were oversimplified, and secondary traces do not have as much geomorphic evidence as the primary traces.			

Notes: A score of 3 indicates high-quality mapping; a score of 1 indicates frequent gaps or mapping errors. We listed both scores for El Mayor–Cucapah due to the score discrepancy. Section S2 of the supplemental text file includes the original reviews (see text footnote 1). Borah Peak-1 and Borah Peak-3 maps were not reviewed.

maps, or aerial photographs. The experts completed their reviews in 4 h and thus spent much less time with the data than the students. We provided the reviewers with a project summary and instructions (see Section S2 of the supplemental text file [footnote 1]). The expert reviewers answered the following questions: (1) Is the mapping complete? (2) Does the geomorphology support the interpreted fault trace(s)? (3) Are the confidence rankings consistent with the geomorphology? (4) What is the overall rating? The reviewers justified their responses, and some provided alternative fault trace interpretations. Section S2 (supplemental text file) includes the full reviews.

■ PRE-RUPTURE MAPPING PERFORMANCE IN PREDICTING COSEISMIC RUPTURES

We developed a qualitative and statistical approach to assess if a coseismic rupture was predicted by a mapped pre-rupture fault trace and to evaluate why unpredicted ruptures were missed (Figs. 3 and 4). We focused on the perspective of whether a coseismic rupture was predicted rather than if a pre-rupture fault trace subsequently ruptured. From an infrastructure risk and public safety perspective, an unexpected surface-fault rupture is much worse than a mapped fault trace that did not rupture. We determined if the earthquake rupture was predicted based on the distance and geomorphic interaction between the rupture trace and mapped fault. We assigned an explanation for unpredicted ruptures and developed summary statistics. The Supplemental Material (see footnote 1) contains the rupture linework with attributes for the rupture prediction and explanation for unpredicted ruptures.

Rupture Prediction and Pre-Rupture Fault Confidence

We assessed rupture prediction by first determining if a rupture and its closest fault were within a threshold distance determined from the fault's confidence ranking (Table 2). These distances roughly reflect the 2σ fault-to-rupture distances from Petersen et al. (2011). If the rupture-to-fault separation distances exceeded the distance threshold, then the rupture was classified as unpredicted. For distances under the threshold, we assessed prediction based on the interaction between the rupture, nearby fault(s), and local geomorphology indicated in the pre-rupture data sets, following Table 2. We subdivided longer rupture segments into lengths rarely less than 100–300 m based on changes in the pre-rupture fault confidence and the geomorphology. The lead author performed this analysis, ensuring a uniform approach for all earthquakes.

Figure 3 shows mapped pre-rupture fault examples by confidence level along with predicted and unpredicted ruptures. In Figures 3A–3B, the strong fault follows a meter-scale topographic step and is separated from the predicted rupture by up to 7 m. In Figures 3C–3D, the strong pre-rupture fault at the hillslope base and the unpredicted rupture located 40 m upslope interact differently with the geomorphology. In Figures 3E–3F, the distinct fault follows

the hillslope and is 25 m from the predicted rupture. In Figures 3G–3H, the distinct fault follows the range-front base at a lower elevation than the unpredicted rupture. The weak fault and predicted rupture (Figs. 3I–3J) cross the hillslope with a separation distance of 12–80 m, which is less than the 100 m threshold distance (Table 2). The unpredicted rupture (Figs. 3K–3L) crosses the braided stream and is 250 m from the mapped weak fault that traces the hillslope base; the threshold distance is exceeded, and the fault and rupture cross different geomorphology. In Figures 3M–3N, a predicted rupture and uncertain fault are separated by up to 50 m along a range front. The proximity and location in the same geomorphic unit indicate prediction. The unpredicted rupture in Figures 3O–3P borders a local depression and is over 100 m from the uncertain fault in the adjacent hills.

Unpredicted Coseismic Rupture Explanations

We developed six categories to explain coseismic ruptures that were unpredicted by the mapped pre-rupture faults (Fig. 4):

- (1) Low mapping resolution: The pre-rupture fault mapping is completed at a low resolution relative to the quality of the available pre-rupture data set and misses observable details (Fig. 4A). This does not include cases of appropriate mapping on low-resolution data sets.
- (2) Low data quality: A strong or distinct pre-rupture fault is mapped through low-quality data or a data hole. The high confidence ranking reflects an error on the part of the mapper who did not understand how to map faults near errors in gridded topography. This explanation most often covers triangulated irregular network errors in digital elevation models (DEMs). An example is the triangles in Figure 4B.
- (3) Wrong or incorrect geomorphic interpretation: Fault geomorphology that offers high-quality fault evidence was misinterpreted. In Figure 4C, the uncertain fault is over 100 m from the sag pond and coseismic rupture. The proximity between the sag pond and rupture is indicative of sag ponds typically being strong indicators of strike-slip faulting.
- (4) Missed geomorphology: There is no mapped pre-rupture fault near a rupture and geomorphology indicative of a strong or distinct fault. The mapper likely missed the tectonic geomorphology or did not identify its importance. Figure 4D shows a missed scarp. This explanation does not include weak lineaments that only indicate a fault with the hindsight of the ruptures, as mapping similar features throughout the mapping area would lead to spurious faults.
- (5) Limited preservation potential: A rupture passes through a very young landscape with a limited potential to preserve tectonic geomorphology. Examples include young alluvial units, marshes, dunes, braided rivers, a construction site, or mine/quarry, although we note that the geometry of these features can be indicative of faulting.
- (6) No unambiguous pre-rupture fault: Examples of this broad category include: (a) bedrock with no fault scarps or other tectonic geomorphology,

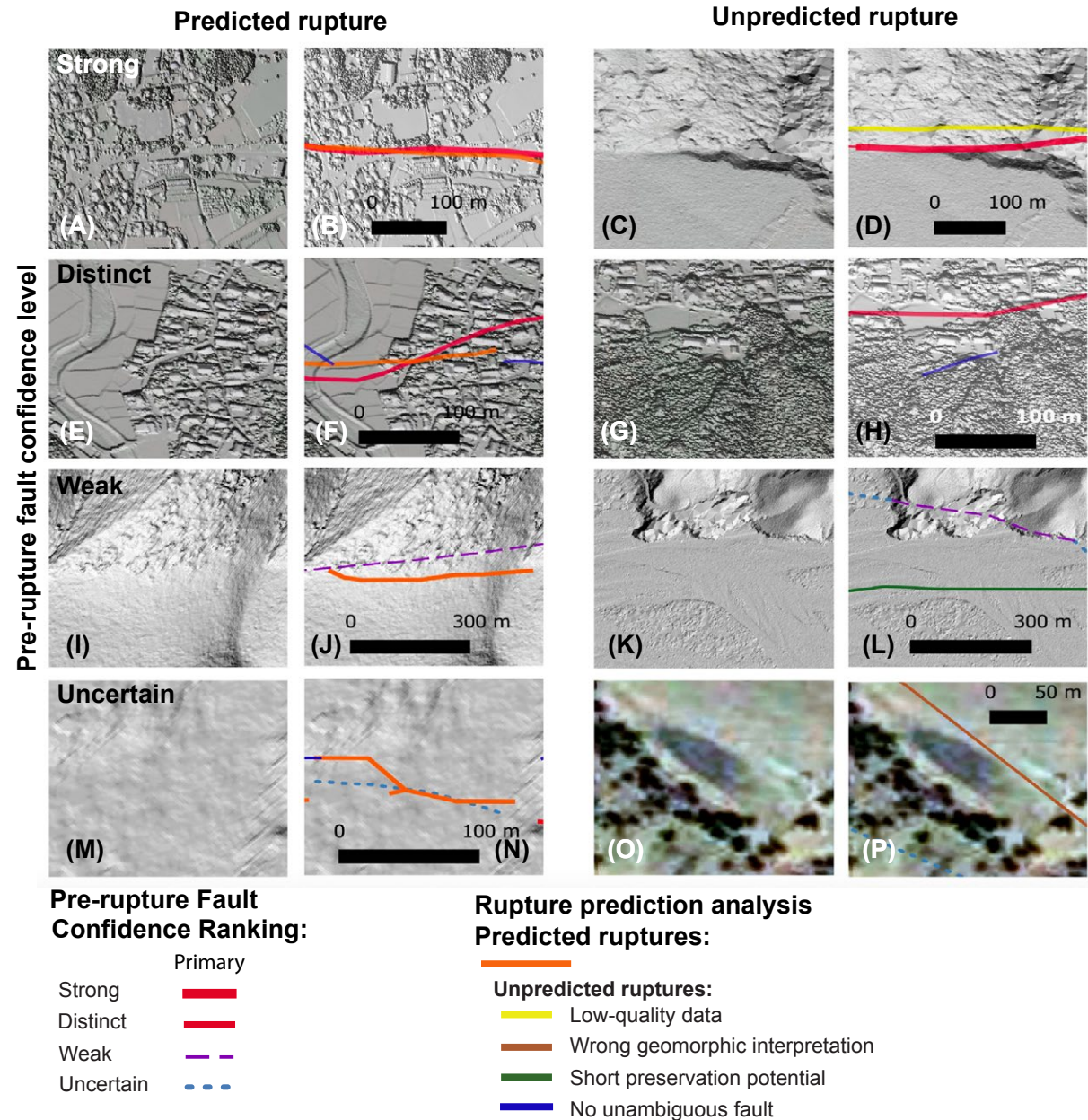


Figure 3. Examples of predicted (left two columns; orange lines) and unpredicted ruptures (right two columns) by pre-rupture fault confidence level on uninterpreted and interpreted remote-sensing data sets.

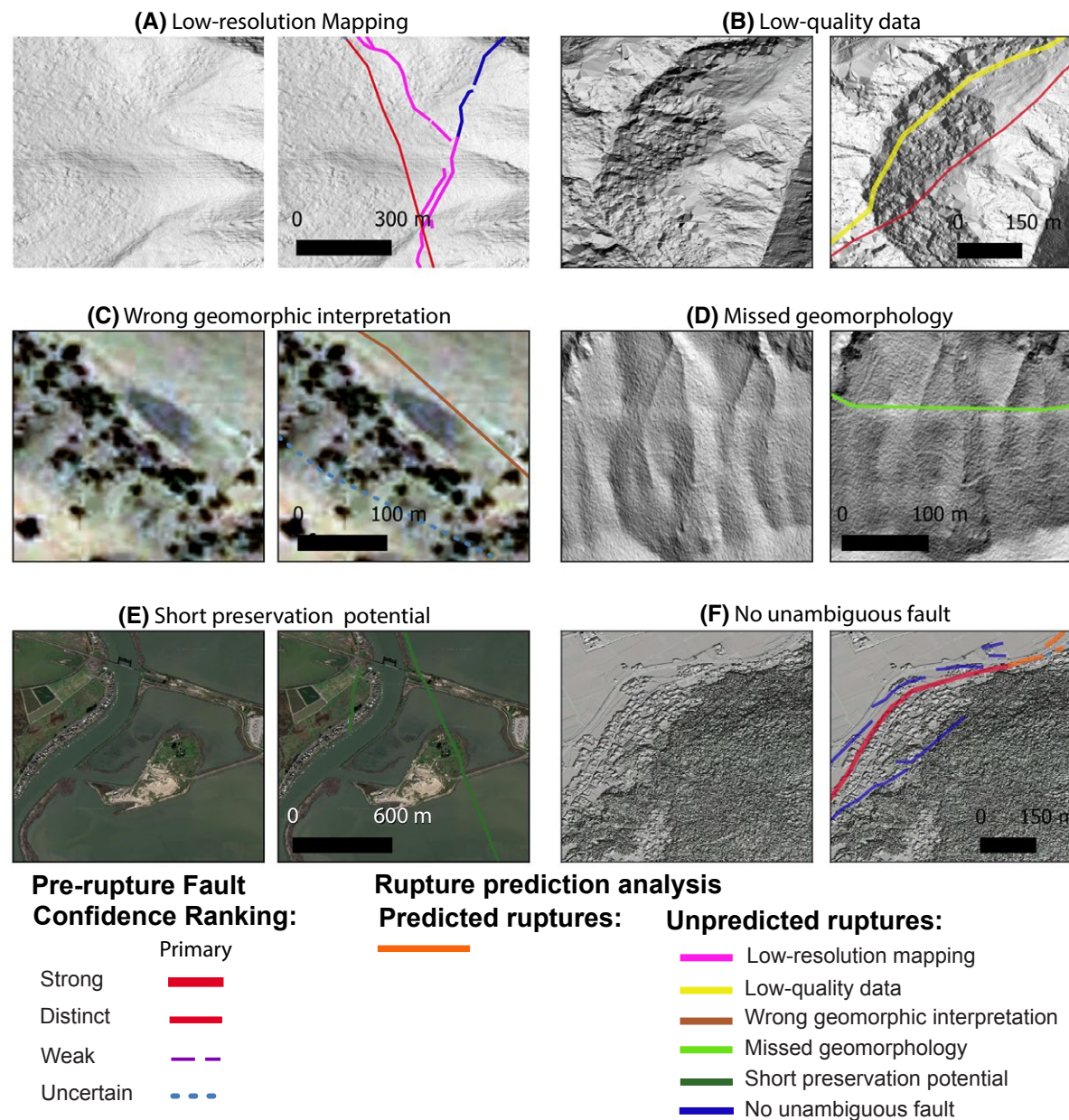


Figure 4. Explanation of unpredicted coseismic ruptures: (A) fault mapping at a low resolution; (B) the strong confidence is too high given the digital terrain model errors; (C) the sag pond adjacent to the rupture should indicate a high-confidence fault; (D) missed rupture crosses the hillslope; (E) missed rupture crosses the marsh with a low preservation potential; and (F) ruptures with no unambiguous pre-rupture fault.

TABLE 2. CRITERIA USED TO ASSESS COSEISMIC RUPTURE PERFORMANCE

Pre-rupture fault confidence	Threshold distance (m)	Pre-rupture fault to coseismic rupture relationship
Strong	50	Fault and rupture pass through the same part of the geomorphic feature with a similar strike.
Distinct	80	Fault and rupture pass through the same geomorphic feature, but the interaction with that feature can differ (e.g., cross different sides of a sag pond).
Weak	100	Fault and rupture may pass near the same geomorphic feature, but the interaction with the feature can differ.
Uncertain	200	Fault and coseismic rupture cross the same geomorphic unit; rupture is predicted within threshold distance so long as there are few to no geomorphic fault indicators.

Notes: The threshold distance is the maximum rupture-to-fault separation distance for predicted ruptures (roughly equal to the 2σ fault-to-rupture separation distances from Petersen et al., 2011). For rupture-to-fault separation distances below the distance threshold, successfully predicted ruptures must also follow the criteria in the third column.

(b) ruptures through a young landscape with low preservation potential, and (c) ruptures with a questionable pre-rupture signal that perhaps could have been predicted with a different landscape geomorphology or fault geometry.

Quantifying Pre-Rupture Mapping Performance

We calculated statistics to quantify: (1) the proportions of coseismic ruptures that were predicted versus unpredicted by the pre-rupture mapping (Table 3), (2) separation distances between predicted ruptures and mapped faults (Table 4), and (3) the frequency of different explanations for unpredicted ruptures (Table 5). We performed the following calculations in Matlab (<https://www.mathworks.com>):

- (1) Coordinate reference system projection: We projected the pre-rupture fault and coseismic rupture linework from World Geodetic System 1984 (WGS84) to the local Universal Transverse Mercator (UTM) zone.
- (2) Linework resampling: We resampled the fault and rupture linework to a 1 m vertex separation, giving each 1 m of fault and rupture length the same weight (Fig. S1).
- (3) Predicted ruptures: Based on our rupture prediction analysis, we calculated the percentage of predicted rupture vertices for all ruptures and by principal or distributed rupture rank (per Sarmiento et al., 2021), shown in the left columns of Table 4. We calculated the summed length of all individual ruptures (middle of Table 3) to illustrate that the summed rupture length often exceeds the along-strike fault length.
- (4) Fault and rupture separation distance: For each rupture vertex, we calculated the distance between the i th coseismic rupture vertex ($x_{co,i}$) and

TABLE 3. MAPPED FAULT TRACE PERFORMANCE BY EARTHQUAKE

Map	Predicted ruptures (%)			Rupture length (km)			Strike length (km)
	All	Principal	Distributed	All	Principal	Distributed	
Borah Peak-1	16	30	5	63	27	33	26
Borah Peak-2	10	20	3	78	34	44	42
Borah Peak-3	43	68	24	72	31	41	36
Parkfield	20	19	93	31	30	1	30
EMC	15	12	16	368	131	236	65
Fukushima	41	41	NA	8.8	8.8	0	8
Napa	51	36	69	54	30	24	22
Kaikoura	29	45	3	34	21	13	19
Kumamoto	35	42	16	22	16	6	18

Notes: Percentage of all, principal, and distributed ruptures predicted by the pre-rupture fault mapping. Rupture length counts the length of all ruptures in the mapping area, and the along-strike length does not count overlapping ruptures multiple times. The along-strike rupture and fault length (Fig. 1) differ if the fault mapping extends beyond the ruptures or if the pre-rupture faults do not include fault tips. EMC—El Mayor—Cucapah; NA—not applicable.

TABLE 4. COSEISMIC RUPTURE AND PRE-RUPTURE FAULT SEPARATION DISTANCES (m)

Predicted rupture	Rupture ranking	Fault confidence	Mean	1-		16th	50th	84th	90th	95th	Mean	σ						
				sided σ									percentile					Log ₁₀
				2-														
Yes	All	All	43	66	79	5	20	69	100	169	1.27	0.61						
		Strong	16	18	25	3	11	27	38	53	0.95	0.54						
		Distinct	16	23	28	3	10	23	33	58	0.93	0.53						
		Weak	30	30	43	5	23	49	56	84	1.25	0.51						
		Uncertain	79	94	123	11	50	134	192	295	1.61	0.56						
	Principal	All	33	42	53	4	18	55	73	123	1.20	0.59						
		Strong	16	16	23	3	11	26	35	47	0.95	0.54						
		Distinct	14	19	23	2	10	21	28	42	0.90	0.52						
		Weak	30	29	41	6	24	48	52	77	1.25	0.50						
	Distributed	Uncertain	62	59	86	10	49	118	168	193	1.55	0.55						
		All	72	103	126	7	32	115	182	375	1.47	0.64						
		Strong	19	26	33	3	9	40	58	82	0.95	0.56						
Distinct		27	36	46	3	13	49	75	110	1.10	0.57							
Weak		33	37	50	22	55	6	67	102	1.25	0.54							
No	All	N/A	621	1059	1228	60	279	1035	1665	2350	2.41	0.60						
	Principal	N/A	414	603	732	48	223	635	989	1931	2.28	0.57						
	Distributed	N/A	959	1475	1760	120	443	1717	2124	3327	2.63	0.58						

Notes: Second-norm statistics (mean and one standard deviation; see Section S6 of the supplemental text file [text footnote 1]), two-sided standard deviation (square-root-square of the mean and one-sided σ which represents the standard deviation with a mean of zero), first-norm statistics (median, 16th, 84th, 90th, and 95th percentiles), and log₁₀ mean and standard deviation for the separation distances between the coseismic ruptures and the mapped pre-rupture fault traces. Statistics are normalized by rupture length, and the three Borah Peak maps collectively have the same weight as each of the other maps. The units of the mean, both standard deviations, and the percentile statistics are meters. The log₁₀ statistics reflect an original unit of meters. N/A—not applicable.

TABLE 5. PERCENTAGE OF UNPREDICTED RUPTURES BY EXPLANATION

Map	Low-resolution mapping			Low data quality			Misinterpreted geomorphology			Missed geomorphology			Low preservation potential			No evidence		
	A	P	D	A	P	D	A	P	D	A	P	D	A	P	D	A	P	D
BP-1	11	28	1	4	0	7	4	10	0	2	5	2	0	0	0	79	57	91
BP-2	0	0	0	0	0	0	3	8	0	8	29	2	0	0	0	89	73	98
BP-3	0	0	0	0	0	0	0	0	0	10	35	2	0	0	0	90	65	90
Parkfield	0	0	0	0	0	0	2	2	0	0	0	0	0	0	0	98	98	100
EMC	0	0	0	0	0	0	0	1	0	4	5	3	5	7	4	91	87	93
Fukushima	0	0	0	0	0	0	0	0	0	0	0	0	0	0	0	100	100	100
Napa	0	0	0	0	0	0	0	0	0	0	0	0	37	48	7	63	52	93
Kaikoura	0	0	0	16	25	9	0	2	0	10	1	18	25	40	12	48	32	61
Kumamoto	0	0	0	0	0	0	0	0	0	0	0	0	0	0	0	100	100	100

Notes: Percentage of unpredicted ruptures by explanation indicated by rupture, arranged by all (A), principal (P), and distributed (D) rank. BP—Borah Peak; EMC—El Mayor-Cucapah.

the closest pre-rupture fault vertex ($x_{pre,i}$, $x_{pre,i}$) by taking the minimum of the second-norm distance between the i th coseismic rupture vertex and all n pre-rupture vertices, as illustrated in Figure S1:

$$\min \left[\sqrt{(x_{co,i} - x_{pre,1:n})^2 + (y_{co,i} - y_{pre,1:n})^2} \right] \quad (3)$$

We assumed that the closest pre-rupture fault vertex was associated with the rupture; we never manually associated faults and ruptures. All distances were positive, and we did not distinguish between ruptures on opposite sides of the fault.

- (5) As shown in Table 4, we calculated multiple statistics that summarized rupture-to-fault distances for all ruptures and faults, by fault confidence, and by rupture ranking. To account for all distances being positive, we converted a one-sided standard deviation to a two-sided standard deviation centered on the fault as discussed in Section S6 of the supplemental text file (see footnote 1), following Petersen et al. (2011). We calculated five percentile (i.e., first-norm) statistics. The logarithm statistics reflect the mean and standard deviation of the \log_{10} value of the rupture-to-fault distances.
- (6) We calculated the percentage of unpredicted ruptures by the six explanations (Table 5).

■ PRE-RUPTURE FAULT MAPPING AND EARTHQUAKE RUPTURE ANALYSIS

In this section, we compare the mapped pre-rupture fault traces with published coseismic ruptures for each earthquake. In Figures 5 through 11, part A is the pre-rupture fault map, part B shows the coseismic ruptures based on the cited study as compiled by Sarmiento et al. (2021), and parts C up to F highlight specific parts of the fault, ruptures, and/or reviewer comments.

1983 M 6.9 Borah Peak, Idaho, Earthquake

The 1983 M 6.9 Borah Peak, Idaho, earthquake (Fig. 5) ruptured 35 km of the Lost River fault with a normal oblique focal mechanism and up to 2.6 m vertical displacement (Doser and Smith, 1985; Crone et al., 1987; DuRoss et al., 2019; Bello et al., 2021). The earthquake propagated to the northwest along the range-bounding Thousand Springs and Warm Springs fault sections and the transbasin, west-striking Arentson Gulch fault in the Willow Creek Hills. We produced three fault maps for Borah Peak (Borah Peak 1–2–3) to explore mapping repeatability. Here, we present Borah Peak-2, which was completed concurrently with the other maps. Figures S2 and S3 show the Borah Peak-1 and Borah Peak-3 fault maps.

For Borah Peak-2, most unpredicted (missed) coseismic ruptures fit into two categories: First, many fault traces were mapped at a scale too broad to capture important fault-related geomorphology in the DSM. Likely, this

oversimplification of the fault trace reflects the mapper's inexperience. In Figure 5C, the mapped fault traces are overly simple given the range-front sinuosity. The distance between the fault and range front varies, and the fault strike and range-front trend are locally inconsistent. Both external reviewers commented on this issue.

Second, missed coseismic ruptures were concentrated in areas of geometric fault complexity. At the southern end of the Warm Springs section, the unpredicted coseismic ruptures cross the foothills and are oblique to the range front (Fig. 5D). These unpredicted ruptures are classified as "no unambiguous fault," reflecting the unclear geomorphic expression. In the transbasin Willow Creek Hills, the mapped fault trace follows the linear drainage and is 1–2 km from the coseismic rupture, which crosses the hills. Paleoseismic studies indicate that only some Lost River fault earthquakes rupture through the Willow Creek Hills (DuRoss et al., 2022), indicating aleatoric variability. The lower frequency of surface ruptures through the Willow Creek Hills may partially explain the inferior geomorphic fault expression compared to the Warm Springs section.

2004 M 6.0 Parkfield, California, Earthquake

The 2004 M 6.0 Parkfield, California, earthquake (Fig. 6) ruptured 32 km of the central San Andreas fault at the partially to fully locked fault transition and is the most recent of several moderate-magnitude Parkfield earthquakes (Bakun et al., 2005). The earthquake is the smallest in our study and produced up to 4 cm of coseismic right-lateral slip (Rymer et al., 2006) and 20 cm of postseismic slip in the 3 mo after the earthquake (Langbein et al., 2006).

A student mapped two primary pre-rupture fault traces located along the Cholame hill front, the Cholame hills, and Middle Mountain with lengths of 20–30 km and predicted 20% of all ruptures. The 2004 earthquake ruptured the Cholame hill front and valley to the southeast and propagated northwest through Middle Mountain. In Cholame, the unpredicted rupture has a straight trace, crosses the valley, runs along the hill front, and is typically 300 m southwest of the mapped fault (Fig. 6B). At the southeast end of Middle Mountain (Figs. 6C–6F), the rupture and mapped fault are 600 m apart. The rupture follows a meter-scale scarp prominent in the post-rupture lidar topography and a vegetation lineament visible in the pre-rupture imagery. The earthquake also ruptured the Southwest fracture zone, a structural domain parallel to the main San Andreas fault. The rupture was unpredicted in this area of relatively poor geomorphic expression, although a scarp and stream-bank exposure show evidence of past faulting (Rymer et al., 2006).

The lack of pre-earthquake meter-scale topographic data made the fault mapping especially challenging. This is surprising, as the San Andreas fault slip rate of ~30 mm/yr presumably drives the development of significant tectonic landforms (Toké et al., 2011). The post-earthquake B4 (Bevis et al., 2005) lidar topography (Fig. 6E) that we reviewed after completing the mapping shows clear faults that very likely were present prior to the 2004 earthquake; the

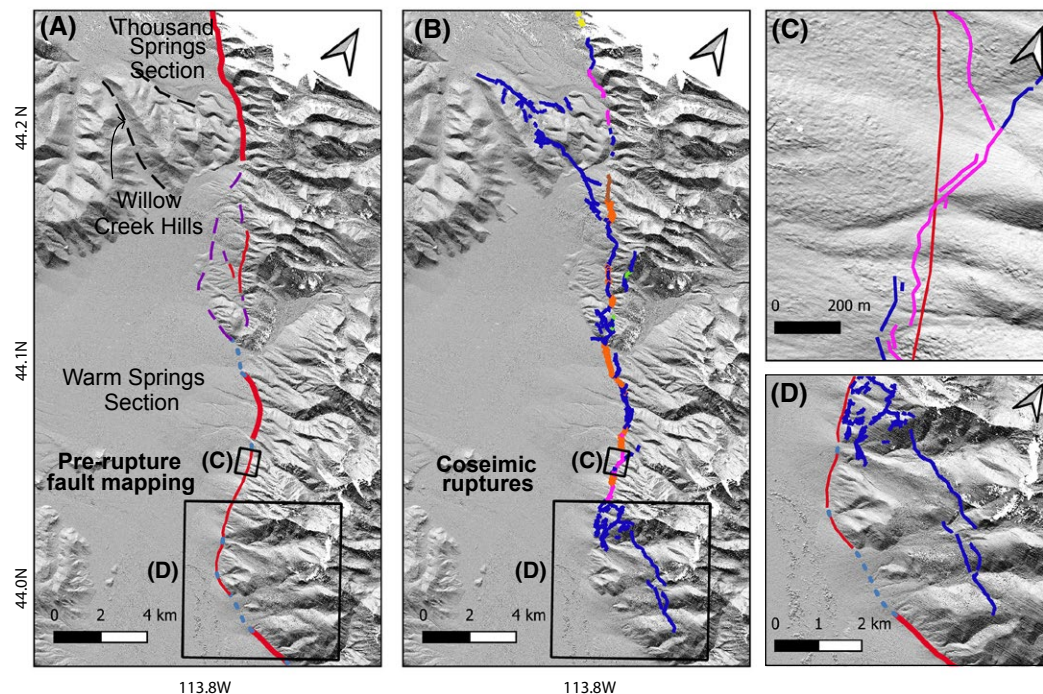


Figure 5. 1983 M 6.9 Borah Peak, Idaho, earthquake: (A) pre-rupture fault (Borah Peak-2) and base hillshade map (Reitman et al., 2015), (B) coseismic ruptures (Crone et al., 1987), (C) low-resolution pre-rupture fault map, which does not predict the range-front coseismic rupture, and (D) the foothill rupture along the segment boundary, which has little to no pre-rupture geomorphic expression.

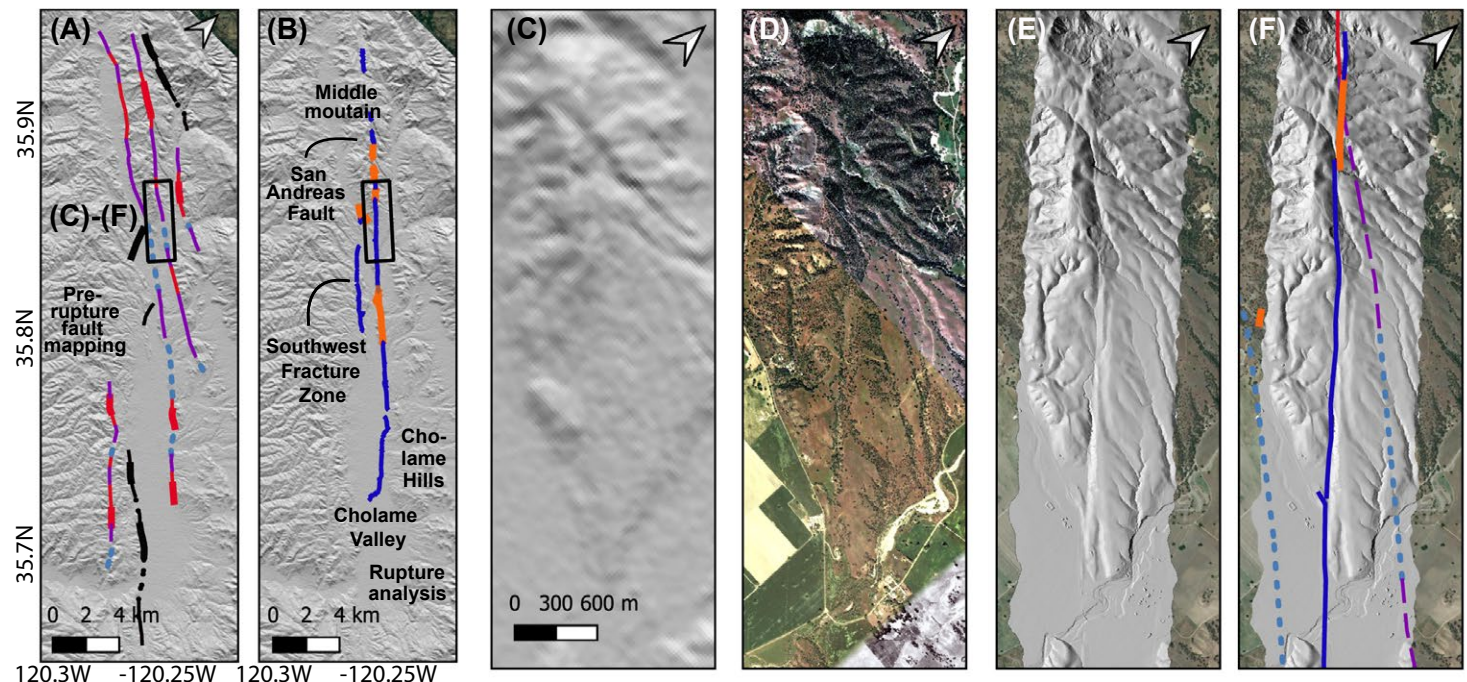
~25 cm of displacement in 2004 likely did not significantly change the fault geomorphology visible in the lidar data. Given the high vegetation and farming activities, we hypothesize that the availability and use of pre-event lidar data would have significantly improved rupture prediction.

2010 M 7.2 El Mayor–Cucapah, Mexico, Earthquake

The 2010 M 7.2 El Mayor–Cucapah earthquake (Fig. 7) ruptured the basin-bounding Laguna Salada fault (Rockwell et al., 2015) and several faults in the Sierra Cucapah and produced up to 2.5 m of right-lateral and 4 m of

oblique slip (Gonzalez-Ortega et al., 2014). Our fault mapping focused on the northwestern 55 km of the 120-km-long rupture. The 1892 M 7.2 Laguna Salada earthquake (Rockwell et al., 2015) produced well-preserved scarps that ruptured again in 2010. The pre-rupture mapping included many 1892 ruptures (Fig. 7C) that ruptured again in 2010. With the exception of the Laguna Salada fault, the 2010 ruptures generally do not follow local topography (Fletcher et al., 2014).

The northwesternmost unpredicted coseismic ruptures are linear and cut Quaternary units but trend oblique to the range front (Fig. 7B). Directly to the south, ruptures are located 100 m upslope of the range front; some of these ruptures were predicted by strong and distinct pre-rupture fault traces, and



Pre-rupture Fault Confidence Ranking:

	Primary	Secondary
Strong		
Distinct		
Weak		
Uncertain		

Rupture prediction analysis:

Predicted ruptures:



Unpredicted ruptures:



Wrong geomorphic interpretation



No unambiguous fault

Figure 6. 2004 M 6.0 Parkfield, California, earthquake: (A) Pre-rupture fault map on a 30 m Shuttle Radar Topography Mission (SRTM) hillshade map, (B) coseismic ruptures (Rymer et al., 2006). (C–F) Middle Mountain inset showing (C) SRTM topography, (D) pre-rupture satellite imagery, (E) post-earthquake 2005 B4 light detection and ranging (lidar) digital terrain model (DTM; Bevis et al., 2005), and (F) B4 DTM with mapped faults and ruptures. Tectonic geomorphology is visible in lidar but not SRTM topography, illustrating the importance of high-resolution data sets for accurate fault mapping.

some parallel ruptures ~1 km to the northeast were predicted by a weak fault. Along the Laguna Salada range-front fault, the mapped pre-rupture fault is continuous, crosses fans of different ages, and steps basinward along the 1892 ruptures. Most of a 7-km-long 2010 rupture in this area was predicted. A secondary fault follows the range-front bend to the southwest, and it ruptured in 1892 but not in 2010. Within the Sierra Cucapah, the mapped pre-rupture

faults have kilometer-scale continuity and sometimes cross deflected streams. The few predicted ruptures follow topographic breaks through sedimentary cover. Mapped pre-rupture faults indicative of novice mapping skill and error include faults that follow streams in the northern Sierra Cucapah, occur along alluvial fan-bedrock contacts near the range front, and trace bedrock contacts lacking fault indicators.

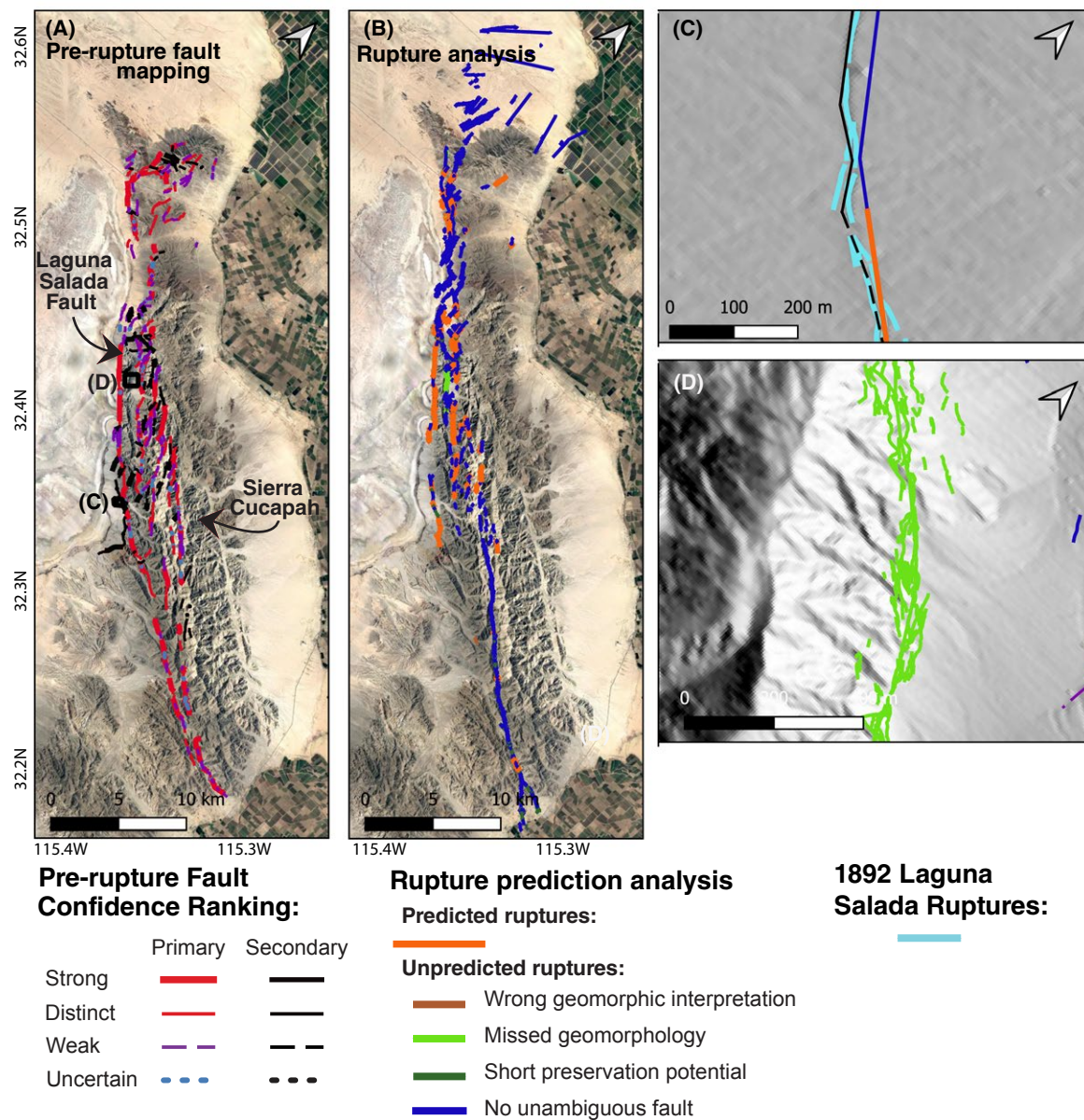


Figure 7. 2010 M 7.2 El Mayor-Cucapah, Mexico, earthquake: (A) pre-rupture fault map, (B) coseismic ruptures (Teran et al., 2015), where the fault traverses through dark-gray bedrock and tan-colored Quaternary alluvial units, (C) partially predicted 2010 ruptures near 1892 M 7.2 Laguna Salada earthquake ruptures (Rockwell et al., 2015), and (D) different mapping scales indicated by the detailed mapping of the coseismic fracture zone, which present challenges to the rupture prediction exercise. Base maps in C and D are 2006 light detection and ranging (lidar) topography (OpenTopography, 2012).

The 6500 coseismic ruptures (Teran et al., 2015), with a total length of 362 km, were mapped from field observations, aerial imagery, lidar topography (Oskin et al., 2012), and displacement maps (Wei et al., 2011). These ruptures were mapped in greater detail than the other rupture maps in our study and highlight varying rupture documentation in the literature (e.g., Sarmiento et al., 2019). The different mapping scales (e.g., Fig. 7D) present a challenge to the rupture prediction exercises. Generally, we grouped whole fault-perpendicular sections either as predicted or unpredicted, which is consistent with the mapper's intent and facilitates a consistent comparison between the pre-rupture fault maps in our study.

2011 M 6.6 Fukushima-Hamadori, Japan, Earthquake

The 2011 M 6.6 Fukushima-Hamadori, Japan, earthquake (Fig. 8) accommodated upper-plate crustal extension following the 2011 Tohoku great earthquake (Kato et al., 2011) in an area of dense vegetation, fluvial modification, and farming activity. The earthquake included 16 km of primary fault rupture with up to 2 m of surface displacement and a 1-km-long branching fault (Nissen et al., 2014).

The main pre-rupture fault is 10 km long, strikes NNW, and is indicated by aligned scarps, oversteepened range fronts, and fluvially modified triangular facets (Fig. 8). In the agricultural fields, the fault was assigned an uncertain confidence where it maintains its range-front strike and connects higher-quality fault indicators. Several other primary faults with lengths up to 4 km follow less prominent geomorphology, often cut across hillslopes, and are indicated by fluvially modified triangular facets and aligned morphology.

In the agricultural fields, the weak and uncertain confidence faults and predicted ruptures are 25–100 m apart. The distinct fault in Figure 8C predicted the rupture. The reviewer suggested that because the fault follows a road cut, the fault may have been mapped in error or may have been assigned a too high confidence. The reviewer was critical of the mapped fault in Figure 8D that follows the valley wall but not a scarp and did not predict the subsequent rupture.

2014 M 6.0 South Napa, California, Earthquake

The 2014 South Napa, California, earthquake ruptured several strands of the West Napa fault (Brocher et al., 2015; DeLong et al., 2016; Ponti et al., 2019) with an ~30-km-long rupture length (Fig. 9). The earthquake produced up to 46 cm of surface displacement, with larger displacements measured along more prominent ruptures and lesser amounts along left-stepping en echelon shears.

The 2014 earthquake ruptured multiple strands that are discontinuous relative to the mapped pre-rupture fault traces (Fig. 9). The four pre-rupture faults (F1–F4) decrease in length toward the southwest: F1 is 25 km long, borders aligned hills, crosses agricultural fields, and crosses the rupture. The uncertain fault confidence in Figure 9C reflects that the stream deflection was possibly

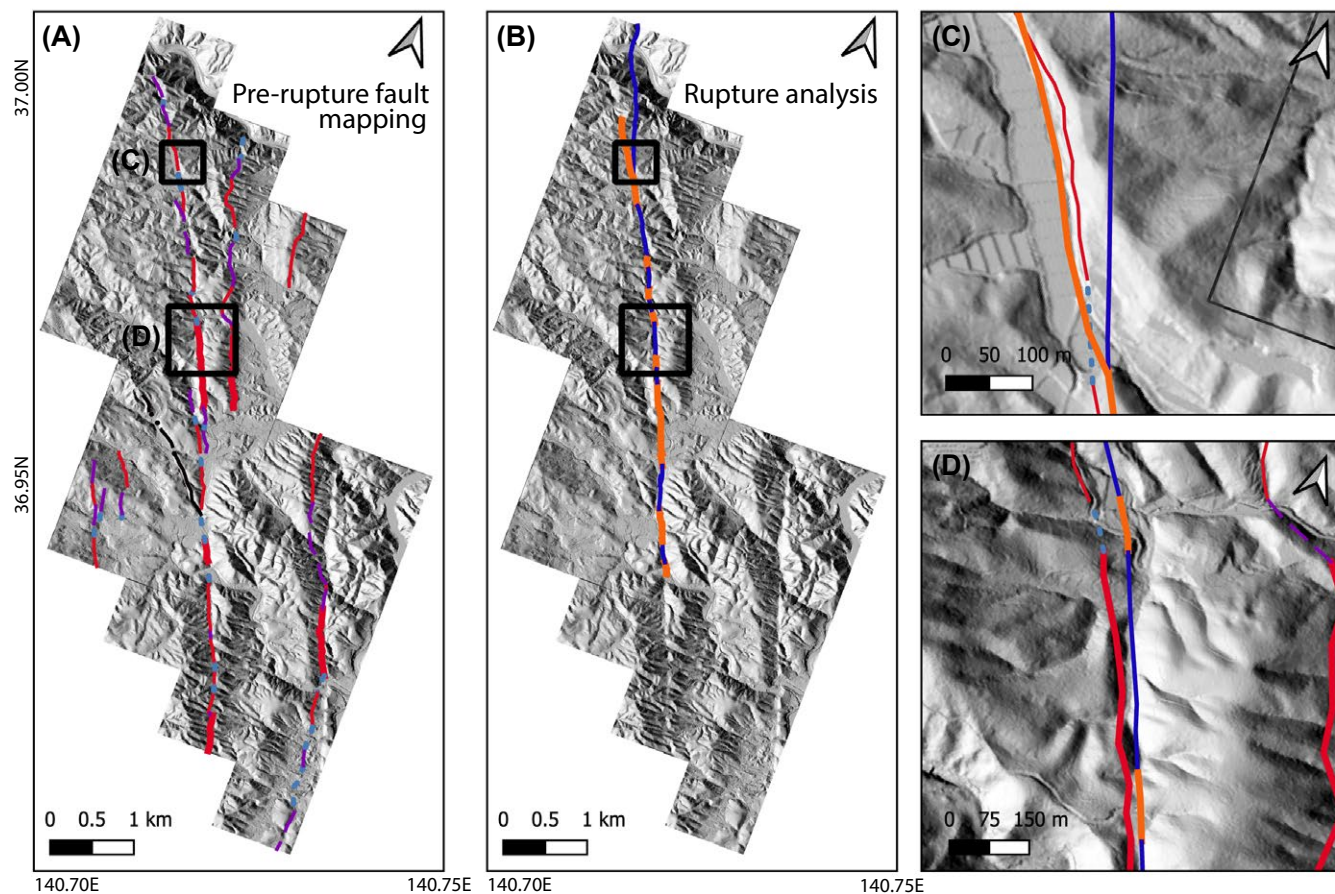
created or accentuated by farming activity; here, the reviewer preferred a higher confidence ranking. While the stream deflection was present as early as 1993 (the earliest Google Earth imagery), no nearby streams show such a deflection, suggesting a nontectonic origin. F2 and F3 pass through agricultural valleys and topographic depressions and along hill fronts. The uncertain pre-rupture faults in suburban areas often predicted ruptures. The higher-confidence faults were across the valley from the unpredicted rupture traces. The reviewer indicated that F4 simply follows a ridgeline and mesa and was likely mapped in error. This view is supported by the observation that F4 did not rupture in 2014. Through the Napa-Sonoma marsh (Fig. 9B), where scarp preservation potential is minimal, the unpredicted coseismic rupture observed with Uninhabited Aerial Vehicle Synthetic Aperture Radar (UAVSAR) data accommodated less than 10 cm of slip (DeLong et al., 2016). The pre-rupture mapping could have been improved by extending the fault along strike through the marsh and assigning a low confidence to this portion of the fault trace.

2016 M 7 Kumamoto, Japan, Earthquake

The 2016 M 7 Kumamoto, Japan, earthquake ruptured 40 km of the Hinagu and Futugawa faults along Japan's Kyushu Island and produced over 2 m of oblique right-lateral slip (Shirahama et al., 2016; Kobayashi, 2017; Scott et al., 2018), as shown in Figure 10. The pre-rupture lidar data (Chiba, 2018) cover the southwestern rupture where the earthquake initiated. The geomorphic environments are broad alluvial plains with active streams and agriculture, intermediate-elevation areas with suburban development, and heavily forested range fronts and hills.

In the southwest, the three subparallel mapped pre-rupture fault traces collectively bound the range front, are concealed under young alluvium, and offset an abandoned terrace. One of the three mapped faults ruptured in 2016. To the northeast, the curvilinear range front is disrupted by drainages and terraces indicating dip-slip faulting. The discontinuous ruptures parallel the range front. Further northeast, the range front becomes steeper, more linear, and locally faceted. The often-discontinuous ruptures concentrate along the range front and were predicted by the mapping. Within the northern portion of the mapping area, unpredicted ruptures form a conjugate shear zone across young alluvial fans. Toward the northeastern edge of the mapping area, several unpredicted ruptures are within 250 m of the range front and coincide with the top of the escarpment. To the north, the weak and uncertain faults follow terrace risers, and their low-quality ranking and the lack of rupture in 2016 reflects that they may be fluvial. The only secondary fault follows an eroded topographic bench to the southeast.

The reviewer suggested edits to the fault trace map completed by the geologic professional, illustrating that well-experienced geologists have different interpretations. In Figure 10C, the predicted ruptures from the consultant mapping are located tens of meters into the valley and reflect observations of the steep, relatively linear, and locally faceted range front. The reviewer's



Pre-rupture Fault Confidence Ranking:

	Primary	Secondary
Strong	—	—
Distinct	- -	- -
Weak	- - -	- - -
Uncertain

Rupture prediction analysis:

Predicted ruptures:	—	Unpredicted ruptures:	—
			No unambiguous fault

Figure 8. 2011 M 6.6 Fukushima-Hamadori, Japan, earthquake: (A) pre-rupture fault map with a digital terrain model (DTM) base map (Nissen et al., 2014), (B) coseismic ruptures from Mizoguchi et al. (2012) and Toda and Tsutsumi (2013), and (C–D) differences between student mapper and expert reviewer interpretations. In C, the reviewer proposed that the rupture-predicting mapped fault followed modified landscapes (agricultural fields and a road) and thus was given too high a confidence. In D, the reviewer indicated that the mapped fault that does not predict the rupture follows the valley wall and not a scarp.

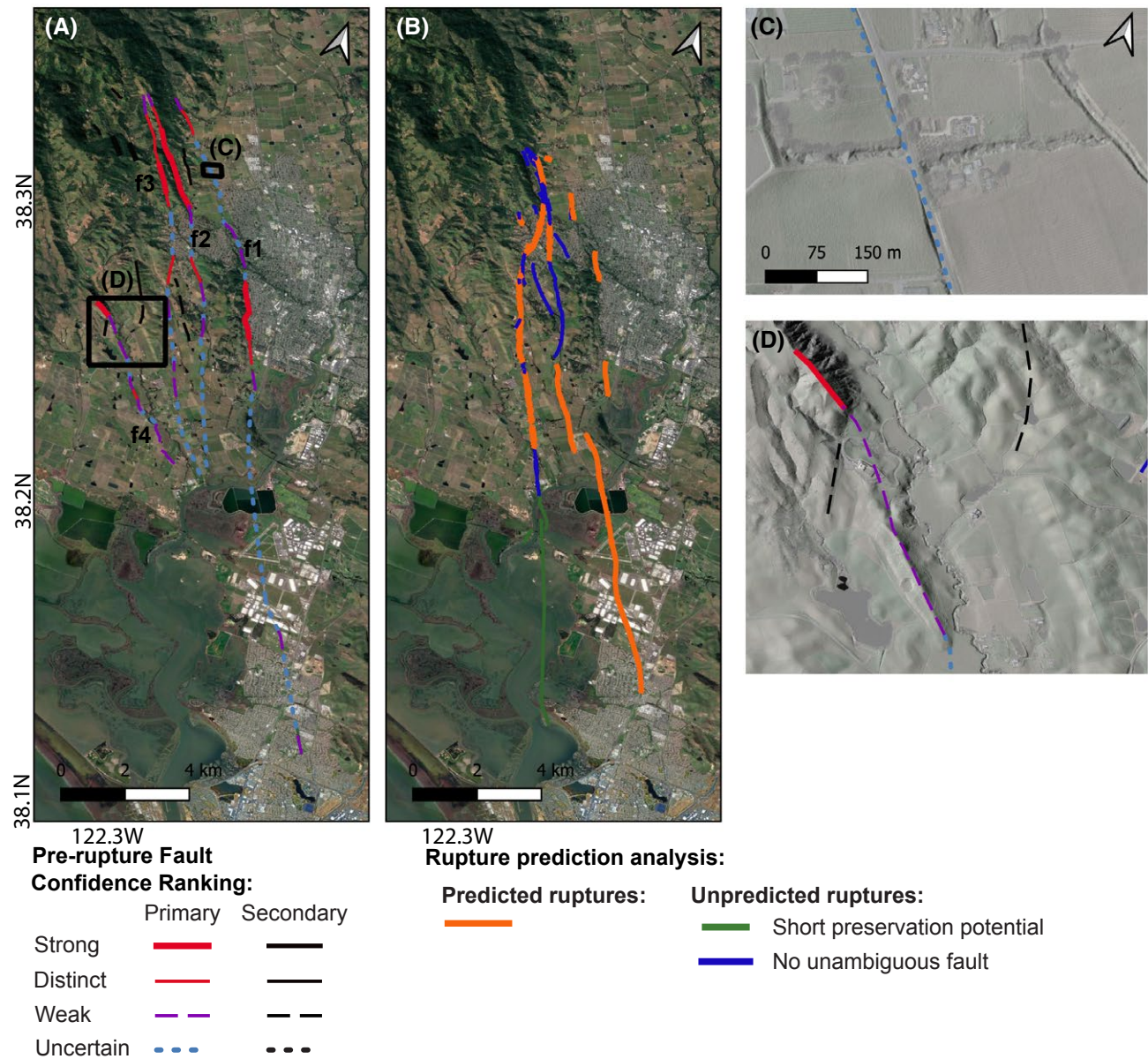
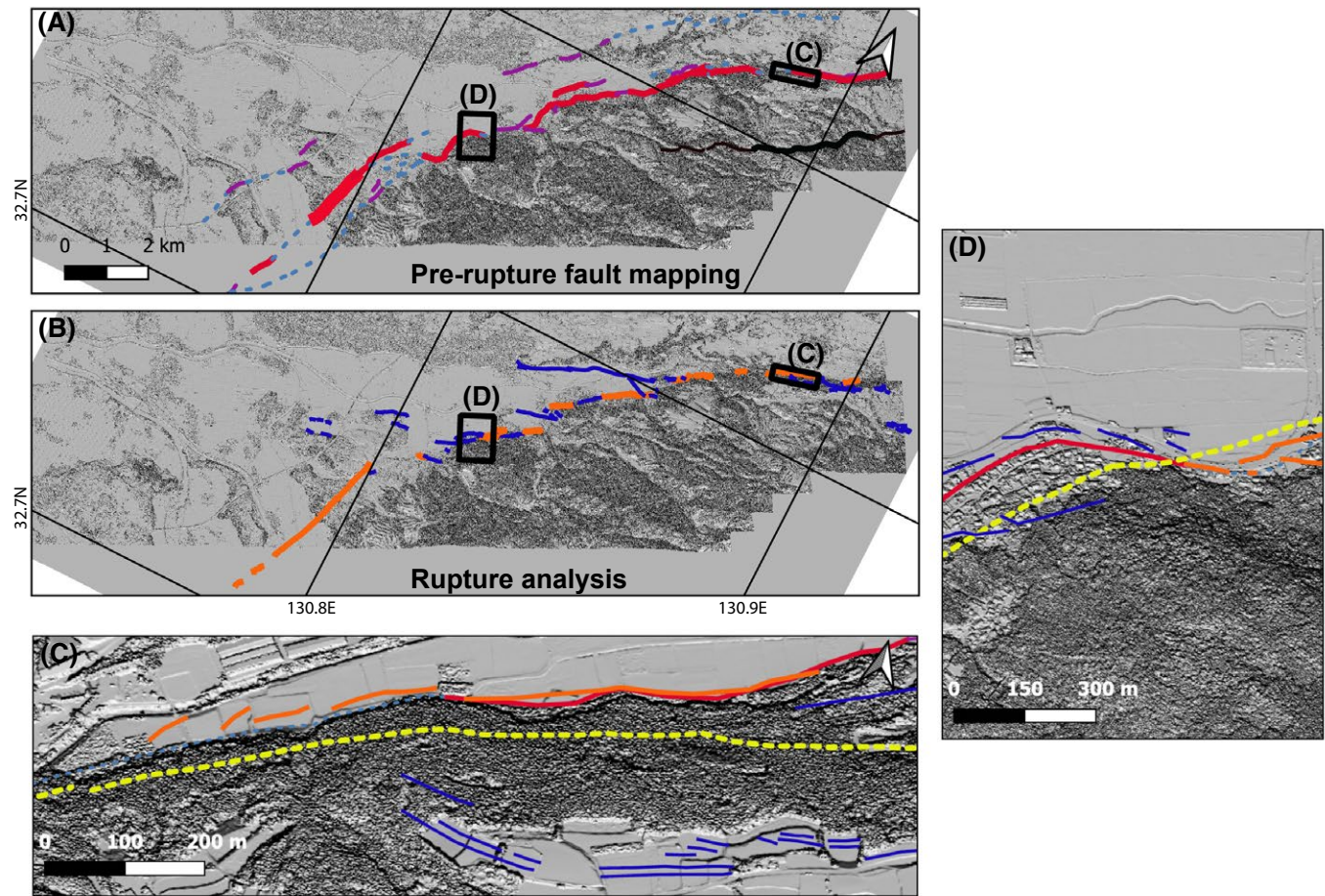


Figure 9. 2014 M 6 South Napa, California, earthquake: (A) pre-rupture fault map with main faults labeled F1–F4, (B) coseismic ruptures from Ponti et al. (2019). (C–D) The reviewer was critical of several mapped faults that did not rupture in 2014. In C, the mapped fault across the deflected stream was mapped as uncertain due to the possible modification from farming activity, but the reviewer preferred a higher ranking. In D, the reviewer was critical of a mapped fault that crosses a mesa and follows a ridgeline but lacks strong fault indicators.



Pre-rupture Fault Confidence Ranking:

	Primary	Secondary
Strong		
Distinct		
Weak		
Uncertain		

Rupture prediction analysis:

Predicted ruptures:



Unpredicted ruptures:

No unambiguous fault

Reviewer faults:



Figure 10. 2016 M 7 Kumamoto, Japan, earthquake: (A) pre-rupture fault map on a light detection and ranging (lidar) digital surface model base map (Chiba, 2018) completed by the geologic professional, (C) coseismic ruptures from Shirahama et al. (2016) and Goto et al. (2017). (C–D) The pre-rupture mapper and reviewer placed faults in different locations near the range front. This highlights different fault location interpretations from expert geologists, emphasizing the need for fault location uncertainty even for maps completed by experts.

upslope fault location would not have predicted the rupture, but this alternative interpretation reflects a common observation of the principal ruptures upslope of the range front (McCalpin, 1987) and possibly also that the reviewer spent much less time with the data set than the geologic professional who completed the map. Figure 10D shows a range-front bend, and the geologic professional's fault follows the contact between the alluvial fan and both the terrace and the range front. The reviewer's fault is straighter and passes along the range front and through the fan. Here, the geologic professional's fault map predicted some of the ruptures, and the reviewer's edits would have performed approximately as well.

2016 M 7 Kaikoura, New Zealand, Earthquake

The 2016 M 7.8 Kaikoura earthquake occurred in the northeastern part of New Zealand's South Island and produced over 1 m of slip on 15 faults (Zinke et al., 2019) with significant strike-slip and reverse components. We mapped a portion of the right-lateral Kekerengu fault where pre-rupture topographic data were available (Fig. 11).

The longest mapped pre-rupture fault trace is 14 km long, strikes ENE, and approximately follows the change from a higher- to lower-relief landscape. Fault indicators include prominent scarps, sag ponds, deflected and beheaded streams, and landslides. Most of this rupture was predicted, and Figure 11C shows an example of a rupture predicted by a strong fault. Unpredicted ruptures are on the opposite side of a sag pond from the fault, are branching, and cross through DTM errors near a strong fault that was assigned too high of a confidence given the DTM errors. To the southwest (Fig. 11D), a 5-km-long, NNW-striking pre-rupture fault often locally borders an alluvial fan and a higher-relief landscape and crosses a braided stream and a hill partially covered with an older landslide. The unpredicted rupture in a braided stream is often hundreds of meters from the fault. Unlike in the Napa-Sonoma marsh in Napa, this rupture could not have been predicted by simply extending a fault along strike.

■ PRE-RUPTURE FAULT MAPPING PERFORMANCE

Coseismic Rupture Prediction

Based on our pre-rupture fault mapping performance assessment, the mapped pre-rupture fault traces predicted a range of 10% to 51% of all ruptures, 12% to 68% of the principal ruptures (Sarmiento et al., 2021), and 3% to 93% of the distributed ruptures (Table 3). The Borah Peak-3 map performed the best for principal ruptures by predicting 68% of their length, and the Napa map performed the best for all ruptures (51% predicted). The Parkfield map predicted 93% of distributed ruptures, but for this earthquake, the ruptures

totaled only 1 km in length. Borah Peak, Kaikoura, and Napa fault maps showed a better prediction of principal ruptures than distributed ruptures, and El Mayor-Cuicapah and Napa fault maps showed the opposite.

We explored potential correlations of rupture prediction with fault and climate properties (Fig. S6). With the exception of Borah Peak-3, rupture prediction generally improved chronologically with earthquake date, indicating the importance of high-quality data (e.g., Treiman et al., 2010). The positive correlation of rainfall (NOAA, 2022; Weather and Climate, 2022) with better rupture prediction could simply be an artifact of our small sample size. Experience sometimes correlated positively with rupture prediction: The senior student (Borah Peak-3) predicted 68% of the ruptures, which is three times as many as the junior student (Borah Peak-1) and twice the other senior student (Borah Peak-2). The consultant's Kumamoto map predicted 42% of primary ruptures, indicating that mapping experience alone cannot be used as a basis to estimate the success in predicting future rupture locations. We found no clear correlation between reviewer ranking, earthquake magnitude, slip sense, or fault slip rate (Scott et al., 1985; Hanks and Schwartz, 1987; Mueller and Rockwell, 1995; Toké et al., 2011; Evans et al., 2012; Little et al., 2018; Ishimura, 2019) and fault mapping performance. We caution that these results may reflect the small sample size and/or the high number of variables.

Fault Trace to Coseismic Rupture Separation Distance

Here, we discuss the rupture-to-fault separation distance based on our pre-rupture fault maps and compare these results to those of Petersen et al. (2011) and the State of California's Alquist Priolo law regarding fault setback distance. Generally, the rupture-to-fault separation distance increased with decreasing fault confidence (Table 4), which is not particularly surprising given the confidence-based distance thresholds for predicted and unpredicted ruptures (Table 2). For predicted ruptures, strong and distinct pre-rupture fault traces had median separation distances of ~10 m and 90th percentile separation distances of ~35 m. Weak and uncertain pre-rupture fault traces, respectively, had approximately twice and five times the separation distance as the strong faults. The distributed rupture separation distances exceeded the principal rupture separation distances, perhaps reflecting the poorer long-term preservation of distributed ruptures.

As shown in Figure 12, the count of both predicted and unpredicted ruptures decreased with distance from the mapped pre-rupture fault, with an approximately linear relationship on a semi-log plot (see also Fig. S4). The portion of coseismic ruptures predicted by strong and distinct pre-rupture faults decayed by several orders of magnitude with increasing separation distances up to ~200 m. For weak and uncertain faults, the decay was more gradual, reflecting the looser criteria for prediction. These relationships can serve as input to calculate the conditional probability of displacement at a site based on the ideal probability distribution function for the fault-to-rupture separation distances (e.g., Youngs et al., 2003; Petersen et al., 2011).

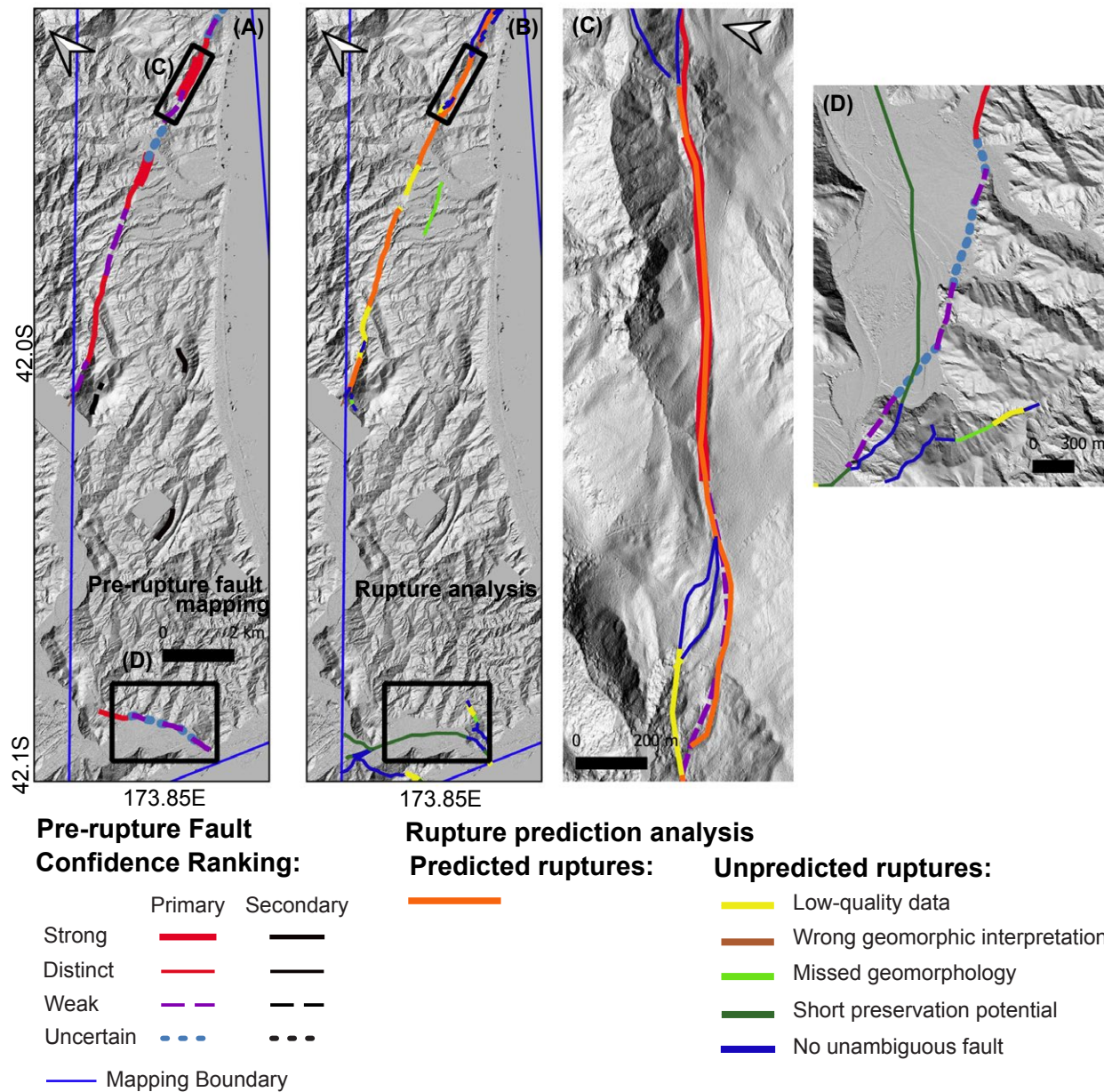


Figure 11. 2016 M 7.8 Kaikoura, New Zealand, earthquake: (A) pre-rupture fault map, (B) coseismic ruptures (GNS Science, 2018; Zinke et al., 2019), (C) a strong pre-rupture fault indicated by scarps, sag ponds, deflected streams, and landslides, and (D; rotated 90°) unpredicted rupture that crosses a braided river with low preservation potential and is located tens to hundreds of meters from the pre-rupture fault mapped along the hill front.

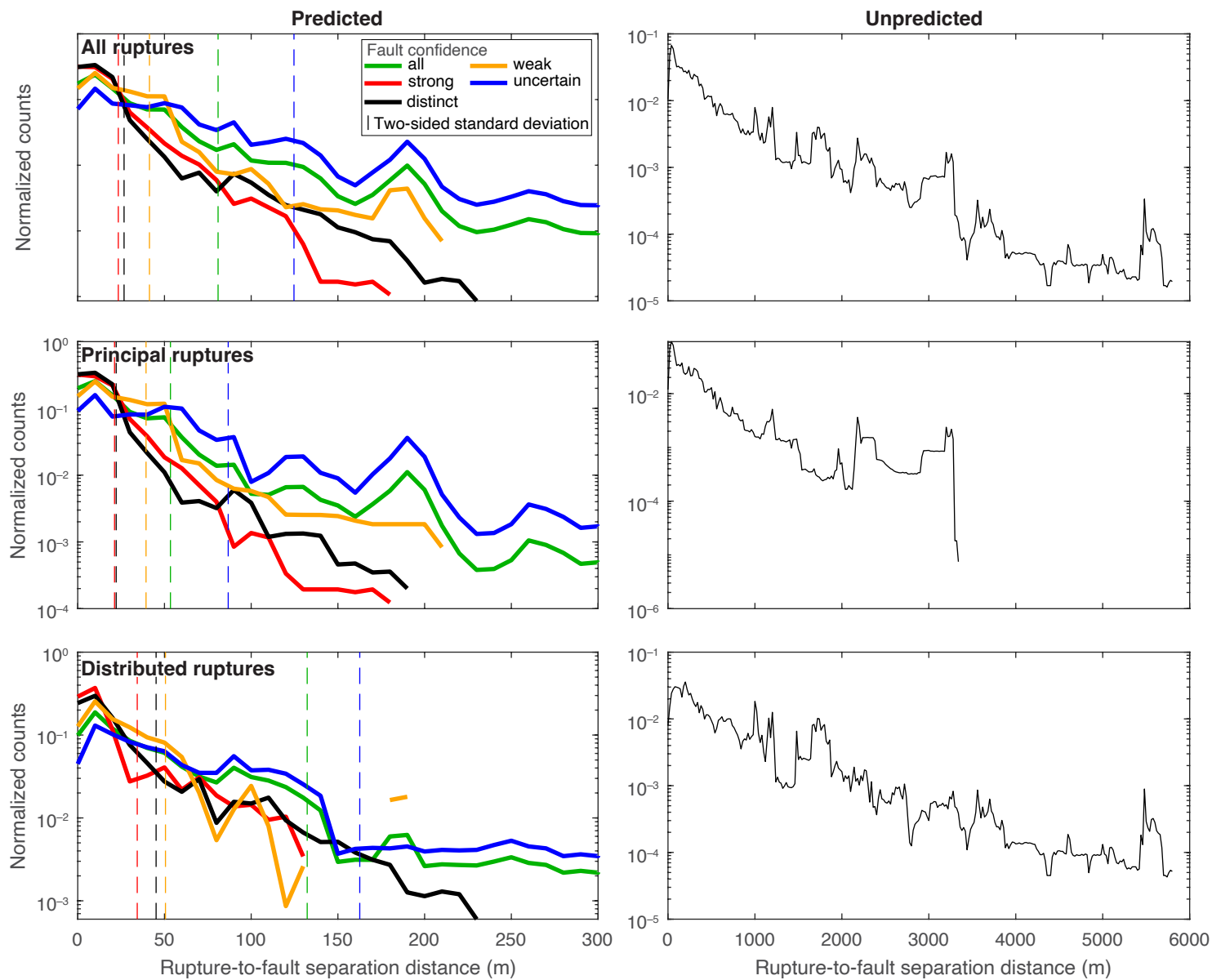


Figure 12. Separation distance between pre-rupture faults and predicted (left) and unpredicted (right) coseismic ruptures by fault confidence with semi-log axes: (top) all ruptures, (middle) principal ruptures, and (bottom) distributed ruptures. The dashed vertical lines are the two-sided standard deviation for the separation distance between the pre-rupture fault and coseismic ruptures.

At least to a first order, our “all rupture” separation distances for predicted ruptures were consistent with those of Petersen et al. (2011), who likely also discounted ruptures far from mapped faults. In detail, the mean fault-to-rupture separation distance from Petersen et al. (2011) for all predicted ruptures was 31 m, while our results showed a median of 20 m and an arithmetic mean of 43 m (Table 4). Our mean separation distances for the three top mapping confidence levels (strong, distinct, weak) were ~80% of the distances calculated by Petersen et al. (2011) for their corresponding mapping accuracy categories (accurate, approximate, concealed). For the lowest-quality fault traces, our 80 m mean separation distance was almost twice as large as distances from Petersen et al. (2011). These observations reflect our restrictive threshold distance requirements for strong, distinct, and weak relative to uncertain fault traces.

Interestingly, the 16 m mean separation distance between predicted ruptures and strong or distinct fault traces was approximately equal to the minimum setback distance of 50 ft (15 m) between faults and newly constructed human-occupied structures required by the Alquist-Priolo Earthquake Fault Zoning Act enacted in 1972 by the California State Legislature (Bryant and Hart, 2007). We note that the minimum setback distance is only granted if confirmatory trench data (i.e., a direct subsurface observation) can preclude faults within 50 ft of the human-occupied structure. Earthquake fault zone boundaries that are used to define areas that require special fault investigations under the Alquist-Priolo Fault Zoning Act commonly have buffer widths of 60–90 m from well-defined minor faults and 150 m from major active faults (California Geological Survey, 2018). The 150 m zone width is similar to our 95th percentile separation distance for all predicted ruptures and all pre-rupture fault confidence levels (169 m).

■ DISCUSSION

Expertise and Fault Mapping

We trained students to create high-quality pre-rupture fault maps that approached the current standard of practice for active fault mapping. We anticipated that students would bring a useful perspective unclouded by prior work. They would view the landscape and interpret active faults without knowledge of specific earthquakes, simulating true pre-rupture fault mapping. To understand the quality of the student mapping, we compared the student and consultant map performance. The consultant’s professional expertise added some value to the rupture prediction (Tables 3–5). The consultant’s Kumamoto map predicted 42% of the principal ruptures, which is the third highest, following Borah Peak-3 (68%) and Kaikoura (45%). Unsurprisingly, students made some mapping errors that would have been reduced or eliminated with additional experience. Errors included mapping at a lower scale than permitted by the data, misinterpreting fault indicators such as sag ponds, and confusing morphometric indicators (e.g., ridgelines) for faults. In contrast, the unpredicted

Kumamoto ruptures in the consultant’s map all lacked clear pre-rupture evidence, indicating no errors. Although imperfect, the student fault maps serve as an important data set to characterize and quantify fault location uncertainty, and their overall quality indicates that the students made substantial improvement in mapping ability over several months of careful teaching.

We explored the poor correlation between the external reviewers’ scores on the pre-rupture fault mapping and the fault performance (Fig. S6C). First, a comparison of the reviewer text and numerical scores illustrated that the reviewers interpreted the provided scoring criteria differently. Second, sometimes the reviewers were critical of a fault’s existence and/or confidence level (and thus likely lowered their scores) in challenging areas, even when the mapped pre-rupture faults predicted the ruptures (e.g., Figs. 8C and 10C). We note that this may reflect the limited time the reviewers had to complete the review. Third, the reviewers judged the fault maps relative to the pre-rupture data sets and thus had the same data-quality limitations as the mappers: The Parkfield pre-rupture fault mapping completed without high-resolution topography was reviewed as “better than adequate” despite only predicting 18% of ruptures. Likely, high-resolution topography data would have improved the mapping.

Geomorphic Indicator Ranking

The GIR serves as a systematic and structured tool (along with morphologic and surficial geologic mapping) to identify fault geomorphology, to rank geomorphic features according to their evidence for faulting, and to assign fault confidence in a repeatable way. The use of the GIR will likely reduce anchoring and confirmation bias in fault maps completed by experts, because the fault map is better supported by geomorphology rather than representing a first interpretation that may be biased by past experience.

In future work, we look toward improving the GIR methodology. First, we anticipate analyzing those GIR features that serve as strong indicators of future coseismic ruptures by analyzing the proximity between GIR features and coseismic ruptures. Second, the ranking system would ideally be augmented to support comparison of fault confidence levels in different tectonic and geomorphic environments. Currently, we normalize the scores locally (Eq. 2), so we cannot compare confidence levels across areas. Third, automation of the confidence ranking calculation based on manually mapped features would reduce the time and potential error in converting mapped GIRs and unranked fault linework to fault linework with confidence rankings.

Challenges in Coseismic Rupture Prediction

The pre-rupture fault mapping performance analysis showed that many coseismic principal ruptures were missed. Even the best results from our experiment revealed that ~30%–50% of principal ruptures were unpredicted.

We discuss several challenges here: mapping error, aleatoric variability, and variability in geomorphic preservation.

Mapping error represents uncertainty associated with fault accuracy and depends on data quality, fault geomorphology clarity, and the geologist's ability to identify and mark geomorphic landforms and integrate these observations into a fault map. Our work largely focused on reducing error by teaching students to identify geologic landforms and map faults while not introducing additional bias or reliance on prior knowledge of mapped events. The first four explanations for unpredicted ruptures (small mapping scale, unappreciated low data quality, wrong geomorphic interpretation, or missed geomorphology) are errors most likely to be made by novice mappers. Knowing to assign a high uncertainty to landscapes with low preservation potential takes insight that we did not have at the start of the project, but it will be straightforward to implement in the future. The three Borah Peak maps indicate that error and map performance likely vary with experience level: The Borah Peak-2 pre-rupture fault map completed by a junior student missed 10 km of principal ruptures due to errors (Tables 3 and 5), while the Borah Peak-3 map completed by a senior student only missed 3 km of principal ruptures due to errors. We note that error can often be further reduced by field reconnaissance or review of other data sets like geologic maps, but these activities would often show the rupture location and therefore would invalidate our simulation of pre-rupture fault mapping.

Natural or aleatoric variability in rupture pattern occurs at several scales. At the narrow scale, paleoseismic trenches are often excavated in areas where localized deformation indicates past ruptures. A trench along the Garlock fault in California showed ruptures from multiple earthquakes over a 25 m width (Dawson et al., 2003), and a trench study compilation in the literature showed a 14–36 m variability in rupture location (Chen et al., 2013). This tens-of-meters scale is similar to the rupture-to-fault separation scale (Table 4). At an intermediate scale, principal ruptures from the 1966 and 2004 M 6 Parkfield earthquakes on Middle Mountain are separated by up to 100 m (Thayer, 2006), exceeding the primary rupture separation statistics herein except for the 84th and higher percentiles of uncertain faults (Table 4). There is uncertainty in which fault strands will rupture at several kilometer scale (e.g., Borah Peak and El Mayor–Cucapah). We decreased the impact of the aleatoric variability at this scale by instructing the students to map in the area with the subsequent ruptures.

While we assumed that past earthquake ruptures are adequately recorded in the landscape, subtle ruptures with low displacement are often buried or eroded (Hemphill-Haley and Weldon, 1999). The relatively high mapping performance in areas with more rainfall (e.g., Kumamoto, Kaikoura, and Fukushima) indicates that a wet climate does not preclude a quality fault map. Limited fault preservation also motivates mapping fault zones instead of distinct faults. The El Mayor–Cucapah fault zone in Figure 10C is ~200 m wide, so a well-positioned fault would be ~100 m away from some ruptures. Rupture zones that are hundreds of meters to a kilometer wide are well documented and should be considered in pre-rupture mapping (e.g., Teran et al., 2015; Rodriguez Padilla et al., 2021, 2022).

We commonly assume that the faults with the strongest geomorphic expression are the most active, but this is not always the case. At Mustang Ridge, California, along the creeping section of the mature central San Andreas fault (Mathews, 1976), the fault steps to the right over a 1-km-wide fault zone marked by an echelon scarps (Rymer et al., 1984; DeLong et al., 2010). Light detection and ranging topographic differencing is consistent with these observations but shows that the trace that accommodated the most creep over the past decade is less geomorphologically distinct than the currently quiescent strand 4 km away (Scott et al., 2020). This highlights the importance of thoroughly scouring the landscape for subtle geomorphic expression of faulting even in areas near faults with prominent geomorphic expression. This also shows that the geomorphology reflects fault activity over the 10^3 – 10^4 yr time scale, which may differ subtly from the current fault activity.

Improving Pre-Rupture Mapping and Rupture Prediction

We identified several approaches to improve fault mapping performance:

- (1) New and higher-quality data will improve pre-rupture fault mapping. Maps based on meter-scale topography correlate with higher rupture prediction performance (Fig. S6). The 2004 Parkfield mapping would likely be improved with lidar topography, as the fault zone is well expressed in lidar data collected in 2005. Projects like the U.S. Geological Survey's 3D Elevation Project (Sugarbaker et al., 2014), which support collection of nationwide high-resolution topography data (primarily derived from lidar), provide essential data for both regional- and local-scale mapping.
- (2) There are several ways to improve pre-rupture fault mapping itself. (a) Reduce mapping errors (Table 5) with our new insights on the common error sources. (b) Mappers stopped fault traces in areas with limited landscape preservation potential due to the lack of fault geomorphology. Instead, these landscapes should be marked with high uncertainty, and faults should be continued along strike, like through the Napa-Sonoma marsh. (c) Research on rupture geometry could give insight into fault behavior in areas of geometric complexity: Biasi and Wesnousky (2017) showed decreased probability of rupture propagation through a 50° or greater bend in a dip-slip fault. For Borah Peak, the rupture is unlikely to pass through the 65° range-front bend immediately south of the rupture (Fig. 5), indicating that mappers should better interrogate the possibility of foothill ruptures oblique to the range front. Earthquakes produce broad deformation zones at range fronts (Beanland et al., 1989; Boncio et al., 2012; Bello et al., 2021), and thus a literature review could indicate rupture zone widths to inform pre-rupture mapping.
- (3) The rupture prediction evaluation in our experiment was based solely on remote-sensing data sets, which differs from typical fault mapping, which uses geologic maps and field reconnaissance. Remote-sensing data lose sensitivity to microtopography and cut exposures observed in the field, and geologic map data provide critical stratigraphic and structural context

for interpreting geomorphology. We anticipate better rupture prediction with additional data such as surface-based field observations, geological maps, and subsurface geophysical data. We plan to explore the utility of some of these other data sets in future work.

Practical Applications

We assessed the accuracy of the pre-rupture fault maps completed in a desktop study using pre-rupture remote-sensing data. Our work informs the

strengths and limitations of this initial desktop mapping to map faults with uncertainty zones for site evaluation, regulatory zoning, and paleoseismic trenching for scientific research. We applied our mapping and rupture statistics (Table 4) to produce fault uncertainty zones for the Borah Peak and Kumamoto map areas and evaluated if these uncertainty zones contained the coseismic ruptures (Fig. 13). To calculate the fault uncertainty zone width (Δf), we used the two-sided standard deviation (Δf) statistics for the four fault confidence rankings distinguished by principal and distributed ruptures:

$$\Delta f = \pm 2\sigma. \tag{4}$$

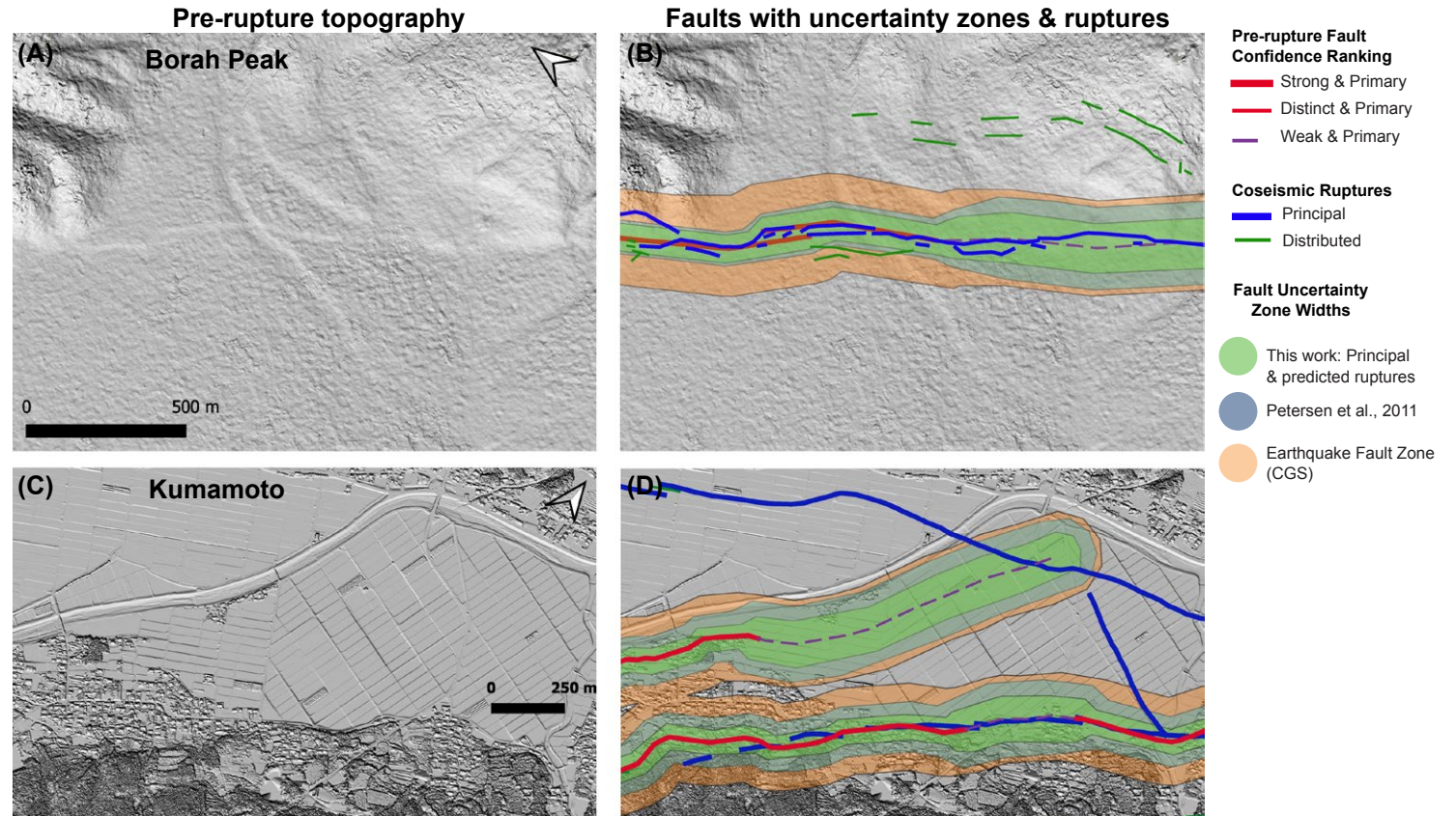


Figure 13. Fault uncertainty zones: uninterpreted topographic hillshade maps for a portion of the (A) Borah Peak and (C) Kumamoto rupture areas, and pre-rupture fault maps from our study for (B) Borah Peak-3 and (D) Kumamoto earthquakes with coseismic ruptures (Crone et al., 1987; Shirahama et al., 2016; Goto et al., 2017). The fault uncertainty zones are from our work (Table 4), the fault-to-rupture statistics presented by Petersen et al. (2011), and the typical widths that the California Geological Survey (CGS) uses to define earthquake fault zones. The presented fault trace linework is from our mapping and was not reviewed by any geological surveys.

If the rupture-to-fault separation distances follow a normal distribution, then Δf spans two two-sided standard deviations on both sides of the fault, and thus there is a 95% chance that a predicted rupture would be in this uncertainty zone. Refer to Section S6 of the supplemental text file for an illustration of this formula.

We compared the fault uncertainty zones from our work (Table 4) to the statistics provided by Petersen et al. (2011) for strike-slip faults and the practice for developing earthquake fault zones outlined by the California Geological Survey (2018). The California Geological Survey's earthquake fault zones are delineated on base maps at a scale of 1:24,000 and have a 150 m buffer from major active faults. The intent of the earthquake fault zone is to mark areas most likely to have active faults and motivate future site investigations but not to predict future rupture locations. We note that our fault maps were not completed or reviewed by any geological survey.

The fault uncertainty zones for pre-rupture fault traces classified as strong and weak for Borah Peak based on our work and the statistics presented by Petersen et al. (2011) are shown in Figures 13A–13B. The zones span the extent of the principal coseismic ruptures. Some of the distributed ruptures west of the principal rupture are within the uncertainty zones. The broader earthquake fault zone includes the principal rupture and the adjacent distributed ruptures. Additional distributed ruptures located ~350 m east of the principal ruptures, however, are outside of all three fault uncertainty zones. For Kumamoto (Figs. 13C–13D), the three fault uncertainty zones for the distinct and uncertain mapped faults at the range front include the majority or all range-front principal ruptures. In the agricultural valley, several ruptures are outside of the fault uncertainty zones, which is not surprising, given the poor fault preservation in the young landscape.

CONCLUSIONS

Accurate prediction of coseismic rupture location before an earthquake is a critical aspect of fault rupture hazard assessment and is an essential step in mitigating the risk of surface-fault displacement for engineered structures that are located across or near active faults. However, accurate fault mapping is challenged by common errors in mapping, aleatoric variability in rupture patterns, and the limited or inconsistent preservation of older ruptures. We assessed mapped pre-rupture fault trace accuracy for predicting ruptures in seven earthquakes. We mentored geoscience students with no prior knowledge of the earthquakes and often limited prior mapping experience as they completed professional-quality fault maps based on pre-earthquake remote-sensing data sets. We developed the geomorphic indicator ranking system to facilitate mapping the geomorphology and fault traces and assigning a confidence level to the fault segments. Using our definitions of acceptable separation distance between fault trace and surface rupture, the mapped pre-rupture fault traces predicted a range of 12% to 68% of the principal rupture lengths. The predicted ruptures were separated on average by a few tens of

meters from well-mapped faults and 100–200 m from uncertain faults. These values inform the development of fault uncertainty zones for displacement hazard applications as well as the accuracy of regional mapping that supports subsequent work on site evaluations, regulatory zoning, and paleoseismic trenching for scientific research.

ACKNOWLEDGMENTS

We acknowledge support for this project from Pacific Gas and Electric, Co. We thank Rui Chen (California Geologic Survey) for insightful conversations during the project and Malinda Zuckerman for feedback on the manuscript. We thank Andrea Hampel (editor), Sean Bemis (reviewer), and an anonymous reviewer for insightful comments during the review process.

REFERENCES CITED

- American Lifelines Alliance, 2005, Seismic Guidelines for Water Pipelines: Oakland, California, American Lifelines Alliance, 256 p.
- Arrowsmith, J.R., and Zielke, O., 2009, Tectonic geomorphology of the San Andreas fault zone from high resolution topography: An example from the Cholame segment: *Geomorphology*, v. 113, p. 70–81, <https://doi.org/10.1016/j.geomorph.2009.01.002>.
- Bakun, W.H., Aagaard, B., Dost, B., Ellsworth, W.L., Hardebeck, J.L., Harris, R.A., Ji, C., Johnston, M.J.S., Langbein, J., Lienkaemper, J.J., Michael, A.J., Murray, J.R., Nadeau, R.M., Reasenberg, P.A., Reichle, M.S., Roeloffs, E.A., Shakal, A., Simpson, R.W., and Waldhauser, F., 2005, Implications for prediction and hazard assessment from the 2004 Parkfield earthquake: *Nature*, v. 437, p. 969–974, <https://doi.org/10.1038/nature04067>.
- Beanland, S., Berryman, K.R., and Blick, G.H., 1989, Geological investigations of the 1987 Edgecumbe earthquake, New Zealand: *New Zealand Journal of Geology and Geophysics*, v. 32, p. 73–91, <https://doi.org/10.1080/00288306.1989.10421390>.
- Bello, S., Scott, C.P., Ferrarini, F., Brozzetti, F., Scott, T., Cirillo, D., de Nardis, R., Arrowsmith, J.R., and Lavecchia, G., 2021, High-resolution surface faulting from the 1983 Idaho Lost River fault Mw 6.9 earthquake and previous events: *Scientific Data*, v. 8, p. 68, <https://doi.org/10.1038/s41597-021-00838-6>.
- Bevis, M., Hudnut, K., Sanchez, R., Toth, C., Grejner-Brzezinska, D., Kendrick, E., Caccamise, D., Raleigh, D., Zhou, H., Shan, S., Shindle, W., Yong, A., Harvey, J., Borsa, A., Ayoub, F., Carter, B., Sartori, M., Phillips, D., and Coloma, F., 2005, The B4 Project: Scanning the San Andreas and San Jacinto fault zones: *American Geophysical Union, Fall Meeting 2005*, abstract H34B–01.
- Biasi, G.P., and Wesnousky, S.G., 2017, Bends and ends of surface ruptures: *Bulletin of the Seismological Society of America*, v. 107, p. 2543–2560, <https://doi.org/10.1785/0120160292>.
- Boncio, P., Galli, P., Naso, G., and Pizzi, A., 2012, Zoning surface rupture hazard along normal faults: Insight from the 2009 Mw 6.3 L'Aquila, central Italy, earthquake and other global earthquakes: *Bulletin of the Seismological Society of America*, v. 102, p. 918–935, <https://doi.org/10.1785/0120100301>.
- Bond, C.E., Gibbs, A.D., Shipton, Z.K., and Jones, S., 2007, What do you think this is? "Conceptual uncertainty" in geoscience interpretation: *GSA Today*, v. 17, no. 11, p. 4–10, <https://doi.org/10.1130/GSAT01711A.1>.
- Bray, J.D., 2001, Developing mitigation measures for the hazards associated with earthquake surface fault rupture, *in* Konagai, K., ed., *A Workshop on Seismic-Fault Induced Failures—Possible Remedies for Damage to Urban Facilities*: Tokyo, Japan, Japan Society for the Promotion of Science p. 55–79.
- Brocher, T.M., Baltay, A.S., Hardebeck, J.L., Pollitz, F.F., Murray, J.R., Llenos, A.L., Schwartz, D.P., Blair, J.L., Ponti, D.J., Lienkaemper, J.J., Langenheim, V.E., Dawson, T.E., Hudnut, K.W., Shelly, D.R., Dreger, D.S., Boatwright, J., Aagaard, B.T., Wald, D.J., Allen, R.M., Barnhart, W.D., Knudsen, K.L., Brooks, B.A., and Scharer, K.M., 2015, The Mw 6.0 24 August 2014 South Napa earthquake: *Seismological Research Letters*, v. 86, p. 309–326, <https://doi.org/10.1785/0220150004>.
- Brooks, B.A., Bevis, M., Whipple, K., Arrowsmith, J.R., Foster, J., Zapata, T., Kendrick, E., Minaya, E., Echalar, A., Blanco, M., Euillades, P., Sandoval, M., and Smalley, R., 2011, Orogenic-wedge deformation and potential for great earthquakes in the central Andean backarc: *Nature Geoscience*, v. 4, p. 380–383, <https://doi.org/10.1038/ngeo1143>.

- Bryant, W.A., and Hart, E.W., 2007, Fault-Rupture Hazard Zones in California, Alquist-Priolo Earthquake Fault Zoning Act With Index to Earthquake Fault Zones Maps: Sacramento, California, California Geological Survey, 42 p.
- California Geological Survey, 2018, Earthquake Fault Zones: California Geological Survey Special Publication 42, 84 p.
- Chen, R., and Petersen, M.D., 2019, Improved implementation of rupture location uncertainty in fault displacement hazard assessment: Bulletin of the Seismological Society of America, v. 109, p. 2132–2137, <https://doi.org/10.1785/0120180305>.
- Chen, R., Dawson, T., and Wills, C.J., 2013, Quantifying Surface Fault Rupture Location Uncertainty for Lifeline Crossings: U.S. Geological Survey National Earthquake Hazards Reduction Program Award Number G11AP20040, https://earthquake.usgs.gov/cfusion/external_grants/reports/G11AP20040.pdf.
- Chiba, T., 2018, Pre-Kumamoto Earthquake (16 April 2016) Rupture Lidar Scan: OpenTopography, <https://doi.org/10.5069/G9XP7303>.
- Cowgill, E., Arrowsmith, J.R., Yin, A., Xiaofeng, W., and Zhengle, C., 2004, The Akato Tagh bend along the Altyn Tagh fault, northwest Tibet 2: Active deformation and the importance of transpression and strain hardening within the Altyn Tagh system: Geological Society of America Bulletin, v. 116, p. 1443–1464, <https://doi.org/10.1130/B25360.1>.
- Coyan, M.M., Arrowsmith, J.R., Umhoefer, P., Coyan, J., Kent, G., Driscoll, N., and Gutierrez, G.M., 2013, Geometry and Quaternary slip behavior of the San Juan de los Planes and Saltito fault zones, Baja California Sur, Mexico: Characterization of rift-margin normal faults: Geosphere, v. 9, p. 426–443, <https://doi.org/10.1130/GES00806.1>.
- Crone, A.J., Machette, M.N., Bonilla, M., Lienkaemper, J.J., Pierce, K., Scott, W., and Bucknam, R., 1987, Surface faulting accompanying the Borah Peak earthquake and segmentation of the Lost River fault, central Idaho: Bulletin of the Seismological Society of America, v. 77, p. 739–770, <https://doi.org/10.1785/BSSA0770030739>.
- Dawson, T.E., McGill, S.F., and Rockwell, T.K., 2003, Irregular recurrence of paleoearthquakes along the central Garlock fault near El Paso Peaks, California: Journal of Geophysical Research: Solid Earth, v. 108, 2356, <https://doi.org/10.1029/2001JB001744>.
- DeLong, S.B., Hilley, G.E., Rymer, M.J., and Prentice, C., 2010, Fault zone structure from topography: Signatures of an echelon fault slip at Mustang Ridge on the San Andreas fault, Monterey County, California: Tectonics, v. 29, TC5003, <https://doi.org/10.1029/2010TC002673>.
- DeLong, S.B., Donnellan, A., Ponti, D.J., Rubin, R.S., Lienkaemper, J.J., Prentice, C.S., Dawson, T.E., Seitz, G., Schwartz, D.P., Hudnut, K.W., Rosa, C., Pickering, A., and Parker, J., 2016, Tearing the terroir: Details and implications of surface rupture and deformation from the 24 August 2014 *M* 6.0 South Napa earthquake, California: Earth and Space Science (Hoboken, New Jersey), v. 3, p. 416–430, <https://doi.org/10.1002/2016EA000176>.
- Doser, D.I., and Smith, R.B., 1985, Source parameters of the 28 October 1983 Borah Peak, Idaho, earthquake from body wave analysis: Bulletin of the Seismological Society of America, v. 75, p. 1041–1051, <https://doi.org/10.1785/BSSA0750041041>.
- DuRoss, C.B., Bunds, M.P., Gold, R.D., Briggs, R.W., Reitman, N.G., Personius, S.F., and Toké, N.A., 2019, Variable normal-fault rupture behavior, northern Lost River fault zone, Idaho, USA: Geosphere, v. 15, p. 1869–1892, <https://doi.org/10.1130/GES02096.1>.
- DuRoss, C.B., Briggs, R.W., Gold, R.D., Hatem, A.E., Elliott, A.J., Delano, J., Medina-Cascales, I., Gray, H.J., Mahan, S.A., Nicovich, S.R., Lifton, Z.M., Kleber, E., McDonald, G., Hiscock, A., Bunds, M., and Reitman, N., 2022, How similar was the 1983 Mw 6.9 Borah Peak earthquake rupture to its surface-faulting predecessors along the northern Lost River fault zone (Idaho, USA)?: Geological Society of America Bulletin, v. 134, p. 2767–2789, <https://doi.org/10.1130/B36144.1>.
- Evans, E.L., Loveless, J.P., and Meade, B.J., 2012, Geodetic constraints on San Francisco Bay area fault slip rates and potential seismogenic asperities on the partially creeping Hayward fault: Journal of Geophysical Research: Solid Earth, v. 117, B03410, <https://doi.org/10.1029/2011JB008398>.
- Farr, T.G., Rosen, P.A., Caro, E., Crippen, R., Duren, R., Hensley, S., Kobrick, M., Paller, M., Rodriguez, E., Roth, L., Seal, D., Shaffer, S., Shimada, J., Umland, J., Werner, M., Oskin, M., Burbank, D., and Alsdorf, D., 2007, The Shuttle Radar Topography Mission: Reviews of Geophysics, v. 45, RG2004, <https://doi.org/10.1029/2005RG000183>.
- Fletcher, J.M., Teran, O.J., Rockwell, T.K., Oskin, M.E., Hudnut, K.W., Mueller, K.J., Spelz, R. M., Alciz, S.O., Masana, E., Faneros, G., Fielding, E., Leprince, S., Morelan, A., Stock, J., Lynch, D., Elliot, A., Gold, P., Liu-Zeng, J., González-Ortega, A., Hinojosa-Corona, A., and González-García, J., 2014, Assembly of a large earthquake from a complex fault system: Surface rupture kinematics of the 4 April 2010 El Mayor–Cucapah (Mexico) Mw 7.2 earthquake: Geosphere, v. 10, p. 797–827, <https://doi.org/10.1130/GES00933.1>.
- Geological Survey of Japan, 1993, Strip Map of the Median Tectonic Line Active Fault System in Shikoku, Japan: Geological Survey of Japan Tectonic Map 8, scale 1:25,000.
- Glennie, C., 2007, Rigorous 3D error analysis of kinematic scanning LIDAR systems: Journal of Applied Geodesy, v. 1, <https://doi.org/10.1515/jag.2007017>.
- GNS Science, 2018, 2016 Kaikoura Rupture: Avalon, New Zealand, GNS Science, <https://data.gns.cri.nz/af/> (last accessed 1 June 2022).
- Gonzalez-Ortega, A., Fialko, Y., Sandwell, D., Alejandro Nava-Pichardo, F., Fletcher, J., Gonzalez-Garcia, J., Lipovsky, B., Floyd, M., and Funning, G., 2014, El Mayor–Cucapah (M_w 7.2) earthquake: Early near-field postseismic deformation from InSAR and GPS observations: Journal of Geophysical Research: Solid Earth, v. 119, p. 1482–1497, <https://doi.org/10.1002/2013JB010193>.
- Goto, H., Tsutsumi, H., Toda, S., and Kumahara, Y., 2017, Geomorphic features of surface ruptures associated with the 2016 Kumamoto earthquake in and around the downtown of Kumamoto City, and implications on triggered slip along active faults: Earth, Planets, and Space, v. 69, p. 26, <https://doi.org/10.1186/s40623-017-0603-9>.
- Goulden, T., and Hopkinson, C., 2010, The forward propagation of integrated system component errors within airborne LIDAR data: Photogrammetric Engineering and Remote Sensing, v. 76, p. 589–601, <https://doi.org/10.14358/PERS.76.5.589>.
- Hall, W.J., Nyman, D.J., Johnson, E.R., and Norton, J.D., 2003, Performance of the Trans-Alaska Pipeline in the November 3, 2002 Denali fault earthquake, in Beavers, J.E., ed., Advancing Mitigation Technologies and Disaster Response for Lifeline Systems: Long Beach, California, United States, American Society of Civil Engineers, p. 522–534, [https://doi.org/10.1061/40687\(2003\)54](https://doi.org/10.1061/40687(2003)54).
- Hanks, T., and Schwartz, D.P., 1987, Morphologic dating of the pre-1983 fault scarp on the Lost River fault at Doublespring Pass Road, Custer County, Idaho: Bulletin of the Seismological Society of America, v. 77, p. 837–846, <https://doi.org/10.1785/BSSA0770030837>.
- Hemphill-Haley, M., and Weldon, R.J., 1999, Estimating prehistoric earthquake magnitude from point measurements of surface rupture: Bulletin of the Seismological Society of America, v. 89, p. 1264–1279, <https://doi.org/10.1785/BSSA0890051264>.
- Honegger, D.G., and Nyman, D.J., 2004, Seismic Design and Assessment of Natural Gas and Liquid Hydrocarbon Pipelines: Houston, Texas, Pipeline Research Council International, Inc., Report L51927.
- Howell, A., Nissen, E., Stahl, T., Clark, K., Kearse, J., Van Dissen, R., Villamor, P., Langridge, R., and Jones, K., 2020, Three-dimensional surface displacements during the 2016 M_w 7.8 Kaikōura earthquake (New Zealand) from photogrammetry-derived point clouds: Journal of Geophysical Research: Solid Earth, v. 125, <https://doi.org/10.1029/2019JB018739>.
- International Atomic Energy Agency, 2021, An Introduction to Probabilistic Fault Displacement Hazard Analysis in Site Evaluation for Existing Nuclear Installations: International Atomic Energy Agency Report IAEA-TECDOC-1987, 134 p., <https://www-pub.iaea.org/MTCD/publications/PDF/TE-1987web.pdf>.
- Isenburg, M., 2019, LAsTools—Efficient Tools for LiDAR Processing: www.lastools.org (last accessed 1 October 2020).
- Ishimura, D., 2019, Co-seismic vertical displacement associated with the 2016 Kumamoto earthquake (M_w 7.0) and activity of the Futagawa fault around Futa, Nishihara Village: Kumamoto Prefecture Active Fault Research, v. 50, p. 33–44.
- Kato, A., Sakai, S., and Obara, K., 2011, A normal-faulting seismic sequence triggered by the 2011 off the Pacific coast of Tohoku earthquake: Wholesale stress regime changes in the upper plate: Earth, Planets, and Space, v. 63, p. 745–748, <https://doi.org/10.5047/eps.2011.06.014>.
- Kerr, J., Nathan, S., Van Dissen, R., Webb, P., Brunson, D., and King, A., 2003, Planning for Development of Land On or Close to Active Faults: A Guide to Assist Resource Management Planners in New Zealand: Wellington, New Zealand, Ministry for the Environment, Report ME 483, 67 p.
- Kobayashi, T., 2017, Earthquake rupture properties of the 2016 Kumamoto earthquake foreshocks (M_j 6.5 and M_j 6.4) revealed by conventional and multiple-aperture InSAR: Earth, Planets, and Space, v. 69, p. 7, <https://doi.org/10.1186/s40623-016-0594-y>.
- Koehler, R.D., Mann, P., Prentice, C.S., Brown, L., Benford, B., and Wiggins-Grandison, M., 2013, Enriquillo-Plantain Garden fault zone in Jamaica: Paleoseismology and seismic hazard: Bulletin of the Seismological Society of America, v. 103, p. 971–983, <https://doi.org/10.1785/0120120215>.
- Langbein, J., Murray, J.R., and Snyder, H.A., 2006, Coseismic and initial postseismic deformation from the 2004 Parkfield, California, earthquake, observed by global positioning system, electronic distance meter, creepmeters, and borehole strainmeters: Bulletin of the Seismological Society of America, v. 96, p. S304–S320, <https://doi.org/10.1785/0120050823>.
- Lienkaemper, J.J., 1992, Map of Recently Active Traces of the Hayward Fault, Alameda and Contra Costa Counties, California: U.S. Geological Survey Miscellaneous Field Studies Map MF-2196, <https://pubs.usgs.gov/mf/1992/2196/>.

- Lienkaemper, J.J., 2006, Digital Database of Recently Active Traces of the Hayward Fault, California: U.S. Geological Survey Data Series 177, <https://doi.org/10.3133/ds177>.
- Little, T.A., Van Dissen, R., Kearsse, J., Norton, K., Benson, A., and Wang, N., 2018, Kekerengu fault, New Zealand: Timing and size of late Holocene surface ruptures: *Bulletin of the Seismological Society of America*, v. 108, p. 1556–1572, <https://doi.org/10.1785/0120170152>.
- Mathews, V., 1976, Correlation of Pinnacles and Neenach volcanic formations and their bearing on San Andreas fault problem: *Bulletin of the American Association of Petroleum Geologists*, v. 60, p. 2128–2141, <https://doi.org/10.1306/C1EA3A82-16C9-11D7-8645000102C1865D>.
- McCalpin, J.P., 1987, Recommended setback distances from active normal faults, in *Proceedings of the Symposium on Engineering Geology and Soils Engineering*: Logan, Utah, Utah State University, p. 35–56.
- McCalpin, J., 2009, *Paleoseismology*: San Diego, California, Academic Press, International Geophysics 95, 692 p.
- Mizoguchi, K., Uehara, S.-i., and Ueta, K., 2012, Surface fault ruptures and slip distributions of the Mw 6.6 11 April 2011 Hamadoori, Fukushima Prefecture, northeast Japan, earthquake: *Bulletin of the Seismological Society of America*, v. 102, p. 1949–1956, <https://doi.org/10.1785/0120110308>.
- Mueller, K.J., and Rockwell, T.K., 1995, Late Quaternary activity of the Laguna Salada fault in northern Baja California, Mexico: *Geological Society of America Bulletin*, v. 107, p. 8–18, [https://doi.org/10.1130/0016-7606\(1995\)107<0008:LQAOTL>2.3.CO;2](https://doi.org/10.1130/0016-7606(1995)107<0008:LQAOTL>2.3.CO;2).
- Nissen, E., Maruyama, T., Ramon Arrowsmith, J., Elliott, J.R., Krishnan, A.K., Oskin, M.E., and Saripalli, S., 2014, Coseismic fault zone deformation revealed with differential LIDAR: Examples from Japanese –7 intraplate earthquakes: *Earth and Planetary Science Letters*, v. 405, p. 244–256, <https://doi.org/10.1016/j.epsl.2014.08.031>.
- National Oceanic and Atmospheric Administration (NOAA), 2022, NOAA National Centers for Environmental Information: Climate Data Online, <https://www.ncei.noaa.gov/cdo-web/> (last accessed 1 June 2022).
- Nurminen, F., Boncio, P., Visini, F., Pace, B., Valentini, A., Baize, S., and Scotti, O., 2020, Probability of occurrence and displacement regression of distributed surface rupturing for reverse earthquakes: *Frontiers of Earth Science*, v. 8, <https://doi.org/10.3389/feart.2020.581605>.
- Nurminen, F., Baize, S., Boncio, P., Blumetti, A.M., Cinti, F.R., Civico, R., and Guerrieri, L., 2022, SURE 2.0—New release of the worldwide database of surface ruptures for fault displacement hazard analyses: *Scientific Data*, v. 9, p. 729, <https://doi.org/10.1038/s41597-022-01835-z>.
- OpenTopography, 2012, 2006 INEGI Sierra Cucupah Empirically Corrected Lidar Dataset: OpenTopography, <https://doi.org/10.5069/G9S180F8> (last accessed 1 September 2020).
- Oskin, M.E., Arrowsmith, J.R., Corona, A.H., Elliott, A.J., Fletcher, J.M., Fielding, E.J., Gold, P.O., Garcia, J.J.G., Hudnut, K.W., Liu-Zeng, J., and Teran, O., 2012, Near-field deformation from the El Mayor–Cucupah earthquake revealed by differential LIDAR: *Science*, v. 335, p. 702–705, <https://doi.org/10.1126/science.1213778>.
- Pamuk, A., Kalkan, E., and Ling, H.I., 2005, Structural and geotechnical impacts of surface rupture on highway structures during recent earthquakes in Turkey: *Soil Dynamics and Earthquake Engineering*, v. 25, p. 581–589, <https://doi.org/10.1016/j.soildyn.2004.11.011>.
- Petersen, M.D., Dawson, T.E., Chen, R., Cao, T., Wills, C.J., Schwartz, D.P., and Frankel, A.D., 2011, Fault displacement hazard for strike-slip faults: *Bulletin of the Seismological Society of America*, v. 101, p. 805–825, <https://doi.org/10.1785/0120100035>.
- Ponti, D.J., Blair, J.L., and Rosa, C.M., 2019, Digital Datasets Documenting Fault Rupture and Ground Deformation Features Produced by the Mw 6.0 South Napa Earthquake of August 24, 2014: U.S. Geological Survey Data Release, <https://doi.org/10.5066/F7P26W84>.
- Rabus, B., Eineder, M., Roth, A., and Bamler, R., 2003, The Shuttle Radar Topography Mission—A new class of digital elevation models acquired by spaceborne radar: *ISPRS Journal of Photogrammetry and Remote Sensing*, v. 57, p. 241–262, [https://doi.org/10.1016/S0924-2716\(02\)00124-7](https://doi.org/10.1016/S0924-2716(02)00124-7).
- Reitman, N.G., Briggs, R.W., Gold, R.D., and DuRoss, C., 2015, Surface deformation associated with the 1983 Borah Peak earthquake measured from digital surface model differencing: *American Geophysical Union, Fall Meeting 2015, abstract T53B-01*.
- Rockwell, T.K., Fletcher, J.M., Teran, O.J., Hernandez, A.P., Mueller, K.J., Salisbury, J.B., Akciz, S.O., and Štěpánčíková, P., 2015, Reassessment of the 1892 Laguna Salada earthquake: Fault kinematics and rupture patterns: *Bulletin of the Seismological Society of America*, v. 105, p. 2885–2893, <https://doi.org/10.1785/0120140274>.
- Rodriguez Padilla, A.M., Quintana, M.A., Prado, R.M., Aguilar, B.J., Shea, T.A., Oskin, M.E., and Garcia, L., 2021, Near-field high-resolution maps of the Ridgecrest earthquakes from aerial imagery: *Seismological Research Letters*, v. 93, no. 1, p. 494–499, <https://doi.org/10.1785/0220210234>.
- Rodriguez Padilla, A.M., Oskin, M.E., Milliner, C.W.D., and Plesch, A., 2022, Accrual of widespread rock damage from the 2019 Ridgecrest earthquakes: *Nature Geoscience*, v. 15, p. 222–226, <https://doi.org/10.1038/s41561-021-00888-w>.
- Rymer, M.J., Lisowski, M., and Burford, R.O., 1984, Structural explanation for low creep rates on the San Andreas fault near Monarch Peak, central California: *Bulletin of the Seismological Society of America*, v. 74, p. 925–931, <https://doi.org/10.1785/BSSA0740030925>.
- Rymer, M.J., Tinsley, J.C., Treiman, J.A., Arrowsmith, J.R., Clahan, K.B., Rosinski, A.M., Bryant, W.A., Snyder, A., Fuis, G., Toke, N.A., and Bowden, G.W., 2006, Surface fault slip associated with the 2004 Parkfield, California, earthquake: *Bulletin of the Seismological Society of America*, v. 96, p. S11–S27, <https://doi.org/10.1785/0120050830>.
- Salisbury, J.B., Haddad, D.E., Rockwell, T., Arrowsmith, J.R., Madugo, C., Zielke, O., and Scharer, K., 2015, Validation of meter-scale surface faulting offset measurements from high-resolution topographic data: *Geosphere*, v. 11, p. 1884–1901, <https://doi.org/10.1130/GES01197.1>.
- Sarmiento, A., Abrahamson, N., Baize, S., Bozorgnia, Y., Chen, R., Coppersmith, K.J., Dawson, T., Donahue, J., Jacob, V., Ketabdard, M., Kottke, A., Kuehn, N., Lavrentiadis, G., Madugo, C., Mazzoni, S., Milliner, C., Shamsaabad, A., Shantz, T., Shen, A., Thompson, S., and Youngs, B., 2019, A new model database for next-generation fault displacement hazard analysis: Seattle, Washington, Seismological Society of America Annual Meeting.
- Sarmiento, A., Abrahamson, N., Baize, S., Bozorgnia, Y., Chen, R., Coppersmith, K.J., Dawson, T., Donahue, J., Jacob, V., Ketabdard, M., Kottke, A., Kuehn, N., Lavrentiadis, G., Madugo, C., Mazzoni, S., Milliner, C., Shamsaabad, A., Shantz, T., Shen, A., Thompson, S., Youngs, B., 2021, Fault Displacement Hazard Initiative Database, <https://www.risksciences.ucla.edu/girs-reports/2021/08> (last accessed 1 June 2022).
- Saviger, R.A.G., 1965, A technique of morphological mapping: *Annals of the Association of American Geographers*, v. 55, p. 514–538, <https://doi.org/10.1111/j.1467-8306.1965.tb00532.x>.
- Scharer, K.M., Weldon, R.J., Fumal, T.E., and Biasi, G.P., 2007, Paleoearthquakes on the southern San Andreas fault, Wrightwood, California, 3000 to 1500 B.C.: A new method for evaluating paleoseismic evidence and earthquake horizons: *Bulletin of the Seismological Society of America*, v. 97, p. 1054–1093, <https://doi.org/10.1785/0120060137>.
- Scott, C.P., Arrowsmith, J.R., Nissen, E., Lajoie, L., Maruyama, T., and Chiba, T., 2018, The M 7 2016 Kumamoto, Japan, earthquake: 3-D deformation along the fault and within the damage zone constrained from differential LIDAR topography: *Journal of Geophysical Research: Solid Earth*, v. 123, p. 6138–6155, <https://doi.org/10.1029/2018JB015581>.
- Scott, C.P., DeLong, S.B., and Arrowsmith, J.R., 2020, Distribution of aseismic deformation along the central San Andreas and Calaveras faults from differencing repeat airborne LIDAR: *Geophysical Research Letters*, v. 47, no. 22, <https://doi.org/10.1029/2020GL090628>.
- Scott, C.P., Phan, M., Nandigam, V., Crosby, C., and Arrowsmith, J.R., 2021, Measuring change at Earth's surface: On-demand vertical and three-dimensional topographic differencing implemented in OpenTopography: *Geosphere*, v. 17, p. 1318–1332, <https://doi.org/10.1130/GES02259.1>.
- Scott, W.E., Pierce, K.L., and Hait, M.H., 1985, Quaternary tectonic setting of the 1983 Borah Peak earthquake, central Idaho: *Bulletin of the Seismological Society of America*, v. 75, p. 1053–1066, <https://doi.org/10.1785/BSSA0750041053>.
- Shirahama, Y., Yoshimi, M., Awata, Y., Maruyama, T., Azuma, T., Miyashita, Y., Mori, H., Imanishi, K., Takeda, N., Ochi, T., Otsubo, M., Asahina, D., and Miyakawa, A., 2016, Characteristics of the surface ruptures associated with the 2016 Kumamoto earthquake sequence, central Kyushu, Japan: *Earth, Planets, and Space*, v. 68, p. 191, <https://doi.org/10.1186/s40623-016-0559-1>.
- Sieh, K.E., and Jahns, R.H., 1984, Holocene activity of the San Andreas fault at Wallace Creek, California: *Geological Society of America Bulletin*, v. 95, p. 883–896, [https://doi.org/10.1130/0016-7606\(1984\)95<883:HAOTSA>2.0.CO;2](https://doi.org/10.1130/0016-7606(1984)95<883:HAOTSA>2.0.CO;2).
- Stepp, J.C., Wong, I., Whitney, J., Quittmeyer, R., Abrahamson, N., Toro, G., Youngs, R., Coppersmith, K., Savy, J., and Sullivan, T., 2001, Probabilistic seismic hazard analyses for ground motions and fault displacement at Yucca Mountain, Nevada: *Earthquake Spectra*, v. 17, p. 113–151, <https://doi.org/10.1193/1.1586169>.
- Stirling, M.W., Abbott, E.R., Rood, D.H., McVerry, G.H., Abrahamson, N.A., Barrell, D.J.A., Huso, R., Litchfield, N.J., Luna, L., Rhoades, D.A., Silvester, P., Van Dissen, R., Van Houtte, C., and Zondervan, A., 2021, First use of fragile geologic features to set the design motions for a major existing engineered structure: *Bulletin of the Seismological Society of America*, v. 111, no. 5, p. 2673–2695, <https://doi.org/10.1785/0120210026>.
- Sugarbaker, L.J., Constance, E.W., Heidemann, H.K., Jason, A.L., Lukas, L., Saghy, D.L., and Stoker, J.M., 2014, The 3D Elevation Program Initiative—A Call for Action: U.S. Geological Survey Circular 1399, 35 pp., <https://pubs.usgs.gov/circ/1399/>.

- Sundermann, S.T., and Kelson, K.I., 2009, Digital Compilation of Central Calaveras Fault Data for the Northern California Map Database: U.S. Geological Survey National Earthquake Hazards Reduction Program 06HQGR0154, https://earthquake.usgs.gov/cfusion/external_grants/reports/06HQGR0154.pdf.
- Teran, O.J., Fletcher, J.M., Oskin, M.E., Rockwell, T.K., Hudnut, K.W., Spelz, R.M., Akciz, S.O., Hernandez-Flores, A.P., and Morelan, A.E., 2015, Geologic and structural controls on rupture zone fabric: A field-based study of the 2010 Mw 7.2 El Mayor–Cucapah earthquake surface rupture: *Geosphere*, v. 11, p. 899–920, <https://doi.org/10.1130/GES01078.1>.
- Thayer, M., 2006, Structural Geology of the San Andreas Fault Zone at Middle Mountain, Near Parkfield, Central California [M.S. thesis]: Tempe, Arizona, Arizona State University, 124 p., http://activetectonics.asu.edu/Parkfield/M_Thayer_MS_2006.pdf.
- Thompson Jobe, J.A., Philibosian, B., Chupik, C., Dawson, T., Bennett, S.E.K., Gold, R., DuRoss, C., Ladinsky, T., Kendrick, K., Haddon, E., Pierce, I., Swanson, B., and Seitz, G., 2020, Evidence of previous faulting along the 2019 Ridgecrest, California, earthquake ruptures: *Bulletin of the Seismological Society of America*, v. 110, p. 1427–1456, <https://doi.org/10.1785/0120200041>.
- Toda, S., and Tsutsumi, H., 2013, Simultaneous reactivation of two, subparallel, inland normal faults during the Mw 6.6 11 April 2011 Iwaki earthquake triggered by the Mw 9.0 Tohoku-oki, Japan, earthquake: *Bulletin of the Seismological Society of America*, v. 103, p. 1584–1602, <https://doi.org/10.1785/0120120281>.
- Toké, N.A., Arrowsmith, J.R., Rymer, M.J., Landgraf, A., Haddad, D.E., Busch, M., Coyan, J., and Hannah, A., 2011, Late Holocene slip rate of the San Andreas fault and its accommodation by creep and moderate-magnitude earthquakes at Parkfield, California: *Geology*, v. 39, p. 243–246, <https://doi.org/10.1130/G31498.1>.
- Toké, N.A., Boone, C.G., and Arrowsmith, J.R., 2014, Fault zone regulation, seismic hazard, and social vulnerability in Los Angeles, California: Hazard or urban amenity?: *Earth's Future*, v. 2, p. 440–457, <https://doi.org/10.1002/2014EF000241>.
- Treiman, J.A., and Bryant, W.A., 2000, Raymond fault, Fault number 103, in *Quaternary Fault and Fold Database of the United States*: U.S. Geological Survey website, <https://earthquakes.usgs.gov/hazards/qfaults> (accessed July 2022).
- Treiman, J.A., Perez, F.G., and Bryant, W.A., 2010, Utility of Combined Aerial Photography and Digital Imagery for Fault Trace Mapping in Diverse Terrain and Vegetation Regimes, in *Digital Mapping Techniques '10—Workshop Proceedings*: U.S. Geological Survey Open-File Report 2012–1171, <http://pubs.usgs.gov/of/2012/1171/>.
- Vedder, J.G., and Wallace, R.E., 1970, Map Showing Recently Active Breaks along the San Andreas and Related Faults between Cholame Valley and Tejon Pass, California: U.S. Geological Survey Miscellaneous Geologic Investigations Map I-574, scale 1:24,000, <https://doi.org/10.3133/i574>.
- Weather and Climate, 2022, Weather and Climate: <https://weather-and-climate.com/average-monthly-precipitation-Rainfall-inches,fukushima-fukushima-jp,Japan> (accessed August 2022).
- Wei, S., Fielding, E., LePrince, S., Sladen, A., Avouac, J.-P., Helmsberger, D., Hauksson, E., Chu, R., Simons, M., Hudnut, K., Herring, T., and Briggs, R., 2011, Superficial simplicity of the 2010 El Mayor–Cucapah earthquake of Baja California in Mexico: *Nature Geoscience*, v. 4, p. 615–618, <https://doi.org/10.1038/ngeo1213>.
- Witter, R.C., Kelson, K.I., Barron, A.D., and Sundermann, S.T., 2003, Map of Active Fault Traces, Geomorphic Features and Quaternary Surficial Deposits along the Central Calaveras Fault, Santa Clara County, California: U.S. Geological Survey National Earthquake Hazards Reduction Program 01HQGR0212, https://earthquake.usgs.gov/cfusion/external_grants/reports/01HQGR0212.pdf.
- Woodward-Lundgren & Associates, 1974, Summary Report: Basis for Pipeline Design for Active Fault Crossings for the Trans Alaska Pipeline System, Appendix A-3.1111: Oakland, California, Woodward-Lundgren & Associates, 115 p.
- Youngs, R.R., Arabasz, W.J., Anderson, R.E., Ramelli, A.R., Ake, J.P., Slemmons, D.B., McCalpin, J.P., Doser, D.L., Fridrich, C.J., Swan, F.H., Rogers, A., Yount, J., Anderson, L., Smith, K., Bruhn, R., Knuepfer, P., Smith, R., dePolo, C., O'Leary, D., Whitney, J., Olig, S., and Toro, G., 2003, A methodology for probabilistic fault displacement hazard analysis (PFDHA): *Earthquake Spectra*, v. 19, p. 191–219, <https://doi.org/10.1193/1.1542891>.
- Zielke, O., Klinger, Y., and Arrowsmith, J.R., 2015, Fault slip and earthquake recurrence along strike-slip faults—Contributions of high-resolution geomorphic data: *Tectonophysics*, v. 638, p. 43–62, <https://doi.org/10.1016/j.tecto.2014.11.004>.
- Zinke, R., Hollingsworth, J., Dolan, J.F., and Van Dissen, R., 2019, Three-dimensional surface deformation in the 2016 M_w 7.8 Kaikōura, New Zealand, earthquake from optical image correlation: Implications for strain localization and long-term evolution of the Pacific–Australian plate boundary: *Geochemistry, Geophysics, Geosystems*, v. 20, p. 1609–1628, <https://doi.org/10.1029/2018GC007951>.